Geochemistry Geophysics Geosystems G3
AN ELECTRONIC JOURNAL OF THE EARTH SCIENCES
Published by AGU and the Geochemical Society

Article
Volume 1, Number 1
23 August 2000
1021, doi:10.1029/2000GC000036
ISSN: 1525-2027

Self-consistent generation of tectonic plates in time-dependent, three-dimensional mantle convection simulations 1. Pseudoplastic yielding

Paul J. Tackley

Department of Earth and Space Sciences, University of California, 405 Hilgard Avenue, Los Angeles, California 90095, USA (ptackley@zepher.ess.ucla.edu)

[1] Presented here are self-consistent, three-dimensional simulations of mantle convection, some of which display an approximation of plate tectonic behavior that is continuous in space and time. Plate behavior arises through a reasonable material description of silicate deformation, with a simple yield stress being sufficient to give first-order plate-like behavior; however, the required yield strength or fault frictional coefficient is much less than experimentally determined values. Toroidal:poloidal ratios are within geologically observed limits. The sensitivity of the system to yield strength and the form of strength envelope is systematically investigated. Optimum plate character is obtained in a narrow range of yield strength, below which diffuse boundaries, and above which episodic behavior, and eventually a rigid lid, are observed. Models with mobile lids develop very long wavelength horizontal structure, the longest wavelength possible in the domain. Two-dimensional models display much greater time dependence than three-dimensional models.

Components: 14,503 words, 21 figures, 1 table.

Keywords: Mantle convection; plate tectonics; rheology; lithosphere.

Index Terms: 8120 Tectonophysics: Dynamics of lithosphere and mantle: general (1213); 8150 Tectonophysics: Plate boundary: general (3040); 8159 Tectonophysics: Rheology: crust and lithosphere (8031); 5475 Planetary Sciences: Solid Surface Planets: Tectonics (8149).

Received 26 December 1999; **Revised** 8 May 2000; **Accepted** 6 June 2000; **Published** 23 August 2000.

Tackley, P. J. (2000), Self-consistent generation of tectonic plates in time-dependent, three-dimensional mantle convection simulations 1. Pseudoplastic yielding, *Geochem. Geophys. Geosyst.*, *1*, 1021, doi:10.1029/2000GC000036.

1. Introduction

[2] Plate tectonics, with attendant continental drift, is arguably the most important manifestation of mantle convection in Earth. However, it has long been a problem that mantle convection calculations with simple viscous, temperature-dependent rheologies do not develop plate tectonics, because such rheologies lack the modes of deformation responsible for the lithospheric strain localization and weakening responsible for plate boundary formation, leading instead to the formation of a global stagnant rigid lid [e.g., *Christensen*, 1984b; *Ogawa et al.*, 1991; *Solomatov*, 1995; *Trompert and Hansen*, 1996]. Thus the general approach to incorporating plates in mantle convection

has been to specify some component of the system (such as plate velocities or weak plate boundaries), while solving for the dynamics of the remainder of the system. While much has been learned by such approaches [e.g., *Bunge and Richards*, 1996; *Davies*, 1989; *Hager and O'Connell*, 1981; *King and Hager*, 1994; *Zhong and Gurnis*, 1995], it is ultimately necessary to understand the formation and evolution of plate boundaries and to incorporate the relevant material properties into numerical models so that plates arise self-consistently from the constitutive equations, rather than being imposed by the modeler. With such self-consistent models, fundamental questions about the nature and evolution of the terrestrial planets Earth, Venus, and Mars, including possible transitions between plate tectonic and non–plate tectonic regimes [*Davies*, 1995; *Moresi and Solomatov*, 1998; *Turcotte*, 1993], could then be answered in a unified and self-consistent framework. For a detailed discussion of the goals, philosophical issues, potential problems, and recent progress toward self-consistent models, the reader is referred to recent reviews [*Bercovici et al.*, 2000; *Tackley*, 2000].

[3] As mentioned above, the inclusion of "realistic" temperature-dependent viscosity leads to a cold upper boundary layer so stiff that it stops moving altogether and forms a rigid (stagnant) lid covering the entire planet, even with power-law "dislocation creep" rheology [*Solomatov*, 1995]. This rigid lid can be thought of as a single plate covering the entire planet, which may be appropriate for Mars or Venus, but not for the Earth. A short-wavelength pattern of upwelling plumes and sheet-like downwellings transports heat to the base of the rigid lid, which it is conducted through, and several works have investigated this style of convection [*Grasset and Parmentier*, 1998; *Moresi and Solomatov*, 1995; *Ratcliff et al.*, 1996, 1997; *Reese et al.*, 1998, 1999b; *Solomatov*, 1995; *Solomatov and Moresi*, 1996; *Trompert and Hansen*, 1998b]. The remainder of this section summarizes our knowledge of lithospheric deformation and describes progress toward incorporating it into numerical models.

1.1. Lithospheric Rheology

[4] The key to understanding Earth's plate tectonics is to understand the mechanisms responsible for the formation of weak plate boundaries. The key processes, which are intrinsically linked, are shear localization and weakening. From field observations, laboratory deformation experiments, and theoretical considerations we have some idea of the deformation mechanisms that may be important in the lithosphere. Although this knowledge is quantitatively not very precise, it is sufficient to allow some first-order investigations of the mechanics of plate formation, such as the study presented here.

[5] The current view of deformation in the oceanic lithosphere (which this paper focuses entirely on) is summarized in the lithospheric strength profile in Figure 1, taken from a review paper by *Kohlstedt et al.* [1995]. Brittle behavior (slip on faults) is dominant in the upper 10–20 km, making a transition to semi-ductile, semibrittle deformation in the midlithosphere, and eventually (at 40 km in the illustrated example) to viscous power-law creep in the lower lithosphere. Lithospheric strength is roughly proportional to depth in the brittle zone (because the frictional strength of faults is proportional to normal stress), a relationship which is often referred to as Byerlee's law [*Byerlee*, 1968]. However, lithospheric strength is only weakly depth dependent in the midlithosphere [*Kirby*, 1980], although the details are not well known. In the viscous lower lithosphere, strength decreases with depth owing to increasing temperature. The strongest part of

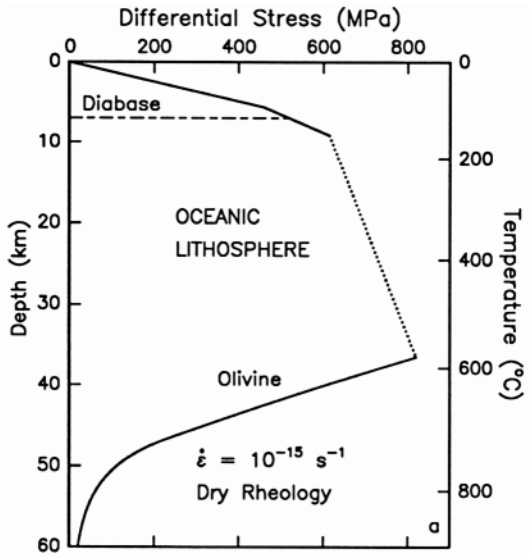

Figure 1. Strength envelope for 60 Myr old oceanic lithosphere [from *Kohlstedt et al.*, 1995] (Figure 9). The solid line in the top part of the lithosphere represents frictional sliding on brittle faults, the solid lines in the bottom part of the figure represent power-law viscous creep, and the dotted line connecting these represents semiductile, semibrittle flow. The transition from brittle to semiductile, semibrittle is known as the brittle-ductile transition (BDT), and the transition from that to viscous creep is known as the brittle-plastic transition (BPT).

the lithosphere is the midlithosphere, deforming by semibrittle, semiductile processes which may be treated at the macroscale as ductile; these processes determine plate strength and may be dominant in the formation of plate boundaries. To summarize, the emerging picture of plate boundaries is one of brittle failure in the top part, with ductile shear zones in the middle lithosphere and ductile power-law flow in the lower lithosphere and upper mantle.

[6] It should be noted that there is a discrepancy between the frictional and yield strengths of rocks as determined by laboratory experiments (Figure 1) and the values required to match large-scale observational constraints. For example, fault frictional coefficients of only 14–30% of experimental values are required in models of crustal deformation in California [*Bird and Kong*, 1994], models of transform fault–bound oceanic plates require exceptionally low fault friction to get platelike behavior [*Zhong et al.*, 1998], and effective lithospheric strengths of only O(100 MPa) are required for supercontinents to break up [*Gurnis*, 1988; *Lowman and Jarvis*, 1999].

[7] The basic strength of oceanic lithosphere discussed above may be further decreased by weakening caused by deformation (i.e., strain weakening), which is thought to play an important role in the formation of weak, localized shear zones. Observations of microstructures from exhumed upper mantle and crustal ductile shear zones [*Drury et al.*, 1991; *Jin et al.*, 1998; *Pili et al.*, 1997; *Sorensen*, 1983; *Vissers et al.*, 1995] indicate that such shear zones are often characterized by very small grains, hydration, and elevated temperatures. Thus the possible mechanisms for their formation are thought to be grain-size reduction, volatile ingestion, and viscous heating, and various analyses have been performed to investigate how localized shear zones may form through one or more of these mechanisms [*Bercovici*, 1998; *Braun et al.*, 1999; *Fleitout and Froidevaux*, 1980; *Kameyama et al.*, 1997; *Regenauer-Lieb*, 1999; *Schubert and Yuen*, 1988; *Yuen et al.*, 1978]. Although viscous deformation is dominant at long timescales, short-timescale elastic processes may be important in forming lithosphere-scale shear zones that subsequently persist over long timescales [e.g., *Regenauer-Lieb and Yuen*, 1998].

1.2. Previous Plate Generation Studies

[8] A number of numerical studies have focused on the possible plate-forming role of various components of the above summarized

lithospheric rheology. Until recently, such studies were restricted to two-dimensional planes representing either a vertical slice through the mantle and lithosphere or a horizontal lithosphere.

[9] Vertical two-dimensional calculations indicated that non-Newtonian, power-law rheologies cause weak zones and strain rate localization above upwellings and downwellings [*Christensen*, 1984a; *Cserepes*, 1982; *Kopitzke*, 1979], resulting in a rudimentary approximation of plates [*Weinstein*, 1996; *Weinstein and Olson*, 1992]. This occurs because the localized buoyancy of upwellings and downwellings causes regions of high stress in the lithosphere above them, resulting in low-viscosity "weak zones" (because power-law rheology gives lower viscosity in regions of high stress). Such calculations were later extended to a more realistic rheology featuring much stronger temperature dependence and weakening that occurred through a depth-dependent yield stress intended to mimic distributed brittle deformation [*Moresi and Solomatov*, 1998], which is important because power-law dislocation creep rheology cannot cause sufficient weakening to generate plate boundaries when more realistic (i.e., very strong) temperature dependence of viscosity is included [*Solomatov*, 1995]. That study delineated the dependence of convective regime on yield stress, finding platelike behavior at low yield values, intermittent lid mobility at intermediate values, and a rigid lid at high values. Low fault frictional coefficients (i.e., <0.1) were needed to obtain platelike behavior, consistent with constraints discussed earlier.

[10] It appears to be fundamentally more difficult to produce plate tectonics in three-dimensional (3-D) geometry, because in addition to convergent and divergent plate boundaries with their associated poloidal motion, Earth also exhibits transform (strike-slip) boundaries, which are associated with toroidal motion [*Hager and O'Connell*, 1978; *Lithgow-Bertelloni et al.*, 1993; *Olson and Bercovici*, 1991]. There are no concentrated local buoyancy forces available to drive and localize deformation at transform boundaries; indeed, buoyancy in the mantle cannot directly drive them at all if the viscosity is purely depth dependent [*Ribe*, 1992].

[11] The problem of transform boundary formation in a two-dimensional sheet representing the lithosphere was examined by *Bercovici* [1993]. Prescribing flow divergence (related to spreading centers) and convergence (related to subduction zones), the rheological conditions necessary for the formation of narrow transform shear zones were examined, both in an idealized Cartesian geometry [*Bercovici*, 1993] and for the present-day configuration of tectonic plates [*Bercovici*, 1995]. Power-law rheology was found to be insufficient to generate narrow transform margins, even with very large values of n, the power-law index. Since power-law rheology with large values of n is similar to pseudoplastic yielding, this implies that pseudoplastic yielding is insufficient to generate narrow transform margins. However, "self-lubricating" rheology, in which stress decreases with strain rate beyond a critical value, produced very sharp transform margins. Self-lubricating rheology may arise through the feedback between viscous dissipation and temperature-dependent viscosity [*Bercovici*, 1996] or by a combination of void production during deformation and ingestion of volatiles [*Bercovici*, 1998]. Indeed, self-lubrication (strain-rate weakening) is a general outcome of combining strain weakening with time strengthening (healing) [*Bercovici*, 1998; *Tackley*, 1998; *Tackley*, 2000] and may thus be applicable to the strong middle lithosphere.

Table 1. Nondimensional Quantities and Dimensional Equivalents

Quantity	non-D to	Value	Dim Value
	Assumed Quantities		
η	η_0	1	10^{23} Pa s
κ	κ	1	10^{-6} m^2/s
k	k	1	3.6 W/m/K
Length	D	1	2.89×10^6m
T	ΔT	1	1300 K
	Derived Quantities		
Heat flux	$k\Delta T/D$	1	1.62 mW/m^2
		50	81 mW/m^2
σ	$\eta_0\kappa/D^2$	1	1.2×10^4 Pa
		10^4	120 MPa
σ'	$\eta_0\kappa/D^3$	1	4.14 Pa/km
		10^6	4.14 MPa/km
		10^6	20.7 MPa/km[a]
v	κ/D	1	0.001 cm/yr
		25	0.025 cm/yr
Time	D^2/κ	1	265 Gyr
		0.04	10.6 Gyr

[a]When scaled by the factor of 5 difference in lithospheric thickness between the model and Earth.

[12] Fully three-dimensional geometry has been considered only recently in three plate studies. Previously, 3-D calculations with mildly temperature-dependent, power-law rheology had indicated some propensity toward transform motion [*Christensen and Harder*, 1991]. The first "plate generation" studies considered the instantaneous flow and lithospheric viscosity structure arising from coupling a 2-D high-viscosity non-Newtonian lithospheric sheet with 3-D buoyancy sources in a constant-viscosity mantle. Good lithospheric plates did not form with power-law [*Weinstein*, 1998] or ductile yield stress [*Tackley*, 1998] lithospheric rheologies, but they did form with a strain-rate weakening (SRW) rheology [*Tackley*, 1998] similar to the "self-lubricating" rheology considered by [*Bercovici*, 1993]. Specifically, broad weak zones with dominant convergent or divergent motion above upwellings and downwellings were interconnected by narrow weak zones with dominant vorticity (indicating strike-slip motion). These results strongly suggested that SRW (or the time-dependent equivalent of strain weakening and healing) is necessary for the formation of tectonic plates, particularly transform boundaries. This conclusion seemed consistent with results from the first 3-D model, which attempted to obtain plate tectonics in a fully time-dependent, self-consistent manner [*Trompert and Hansen*, 1998a]. The model assumed a ductile yield stress that is constant with depth (representing midlithosphere ductile deformation) and exhibited mainly rigid-lid convection, with occasional, tantalizing bursts of localized platelike behavior associated with part of the rigid lid collapsing into the interior.

[13] Thus previously published 3-D plate generation models either are instantaneous or give only intermittent, localized platelike behavior. In this paper are presented the first self-consistent, time-dependent, three-dimensional models in which plates exist and evolve continuously in space and time. A preliminary model with these characteristics and related to those presented here was first published by *Tackley et al.* [1999]. This paper focuses on the role of a

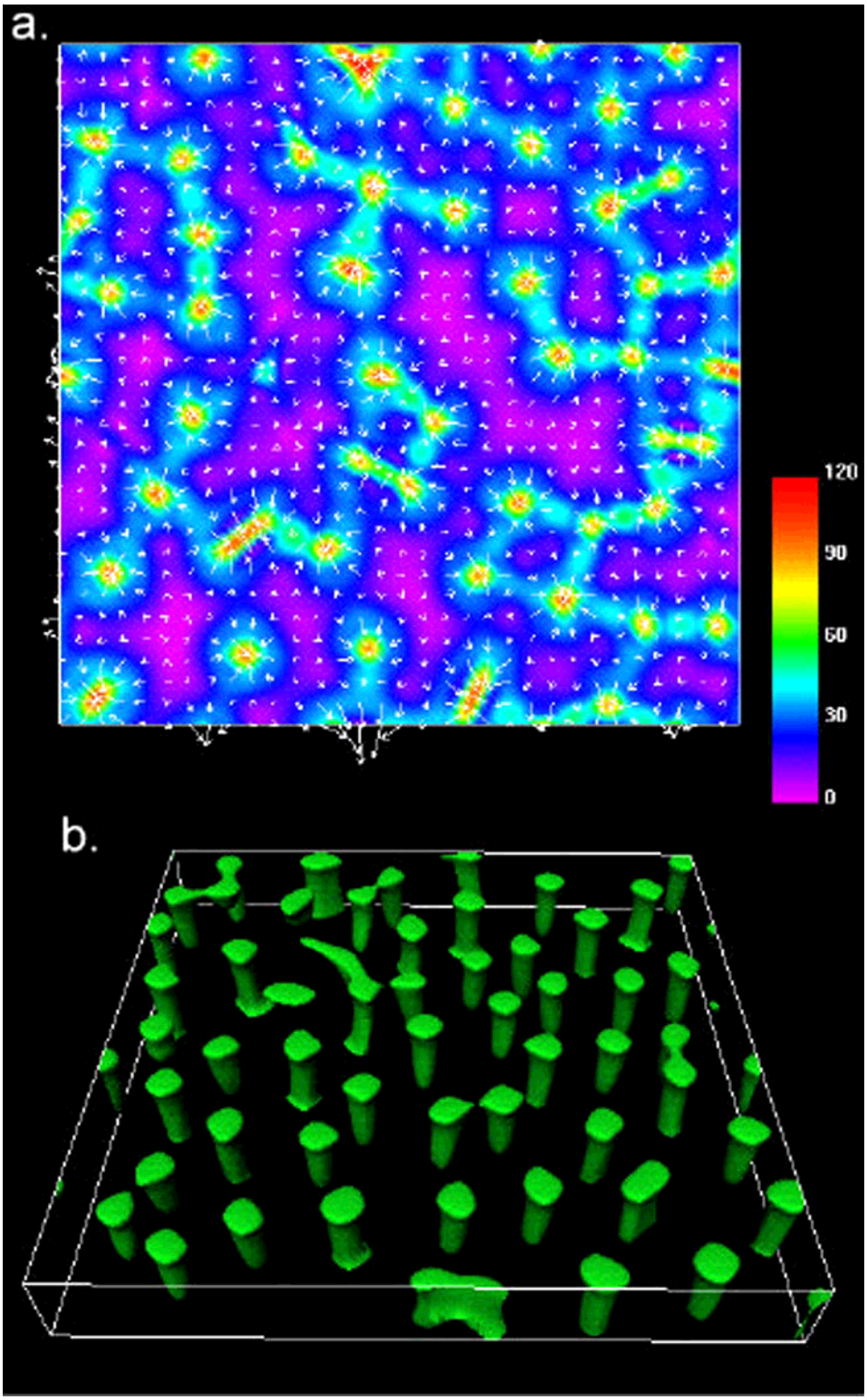
a.
120
90
60
30
0
b.

viscoplastic yield stress combined with temperature-dependent viscosity; a companion paper (''part 2'') adds the effects of strain weakening and depth-dependent viscosity.

2. Model

2.1. Equations

[14] For simplicity, the Boussinesq approximation is adopted. The usual nondimensional equations expressing conservation of mass, momentum, and continuity are

$$\underline{\nabla} \bullet \underline{v} = 0, \tag{1}$$

$$\begin{aligned} \underline{\nabla} \bullet \underline{\underline{\sigma}} - \underline{\nabla} p &= Ra\ T \underline{\hat{z}}; \\ \sigma_{ij} &= \eta(v_{i,j} + v_{j,i}) \equiv 2\eta \dot{\varepsilon}_{ij}, \end{aligned} \tag{2}$$

$$\frac{\partial T}{\partial t} = \nabla^2 T - \underline{v} \bullet \underline{\nabla} T + H, \tag{3}$$

where the various quantities, nondimensionalized to the conventional thermal scales [*Tackley*, 1996a], are velocity $\underline{v}$, deviatoric stress tensor $\underline{\underline{\sigma}}$, pressure p, temperature T, vertical unit vector $\underline{\hat{z}}$ (up being positive), time t, internal heating rate H, strain rate tensor $\underline{\underline{\dot{\varepsilon}}}$, and viscosity η. Ra is the temperature-based Rayleigh number defined as

$$Ra = \frac{\rho g \alpha \Delta T D^3}{\eta_0 \kappa}, \tag{4}$$

where ρ, g, α, ΔT, D, κ, and η_0 are density, gravitational acceleration, temperature scale, depth of layer, thermal diffusivity, and reference viscosity, respectively. The cases presented in this paper are entirely heated from within, with the core-mantle boundary (CMB) set to be insulating (zero heat flux) rather than isothermal. The parameters Ra and H are chosen to give internal temperatures which are approximately 1, thus maintaining a meaningful temperature scale (i.e., T = 1 can be thought of as the mantle potential temperature of around 1600 K) and facilitating direct comparison with similar basally heated cases (not presented here) without having to rescale all of the parameters to a different nondimensionalization, as would be the case if a temperature scale based on internal heating rate were chosen [e.g., *Parmentier et al.* [1994]. The internal heating Rayleigh number is given by

$$Ra_H = Ra\ H. \tag{5}$$

2.2. Rheology

[15] The key parameter in this study is the ''effective'' viscosity, which can be a function of temperature, depth, and strain rate. The rheological model for combining these complexities is based on that suggested by *Tackley* [2000]. The starting point is an Arrhenius-type temperature-dependent viscosity law:

$$\eta(T) = \exp\left[\frac{23.03}{T+1} - \frac{23.03}{2}\right], \tag{6}$$

giving a variation of factor 10^5 between nondimensional temperatures of 0 and 1. The viscosity is equal to 1.0 at T = 1, the ''typical'' internal temperature, rather than using the ''surface'' value, which is very poorly defined for a real planet (somewhere between 10^{40} and 10^{70} Pa s using typical olivine activation energies). The chosen viscosity variation is much less than realistic because numerical problems frequently occur for much larger variations, but it is sufficiently high to give the rigid lid mode in the absence of other complexities.

[16] Consistent with the lithospheric strength profile discussed earlier and in Figure 1, a two-component yield stress is assumed, with a depth-dependent component to represent brit-

Figure 2. Constant-viscosity, internally heated convection: (a) Surface strain rate and (b) isosurface showing cold downwellings where the temperature is 0.1 lower than the geotherm.

tle processes and a constant component to represent semiductile, semibrittle processes:

$$\sigma_y(z) = \min[(1-z)\sigma'_{y\_\text{brittle}}, \sigma_{y\_\text{ductile}}], \quad (7)$$

where $\sigma_{y\_\text{ductile}}$ is the constant yield stress and $\sigma'_{y\_\text{brittle}}$ is the gradient of brittle yield stress with depth (z = 1 at the surface and 0 at the CMB). The yielding is implemented by means of an effective viscosity, defined as

$$\eta_{\text{eff}} = \min\left[\eta(z,T), \frac{\sigma_y(z)}{2\dot{\varepsilon}}\right], \quad (8)$$

where $\dot{\varepsilon}$ is the second invariant of the strain rate tensor:

$$\dot{\varepsilon} = \sqrt{\dot{\varepsilon}_{ij}\dot{\varepsilon}_{ij}} \quad (9)$$

Although (7) and (8) imply zero viscosity at the surface, this does not happen in practice because viscosity is calculated at the cell centers (the shallowest of which is 1/2 grid spacing inside the domain) and because viscosity is truncated to a minimum of 0.1.

[17] The final step in calculating the viscosity field is to truncate viscosities to be between 10^4 and 0.1, in order to avoid numerical difficulties.

2.3. Domain

[18] A periodic Cartesian domain of aspect ratio 8 was assumed. This aspect ratio may be similar to the "effective" aspect ratio of the spherical Earth, although there is not a unique way of determining this: Dividing the circumference of the planet at midmantle depth by the mantle depth yields an aspect ratio of 10.7, whereas matching the volume:depth ratio yields an aspect ratio 6.1. Upper and lower boundaries are free-slip, with the top boundary isothermal (T = 0) and the lower boundary zero heat flux.

2.4. Numerical Method

[19] Solutions were obtained using the finite volume, primitive-variable multigrid code STAG3D, which is described elsewhere [*Tackley*, 1993, 1994, 1996a]. A major problem with multigrid solution methods is that successive iterations (V cycles) may fail to converge when large viscosity variations are present, thus limiting the viscosity contrast that can be modeled. The reason for this is that corrections calculated on coarse grids may be inaccurate, because the viscosity variations are not "seen" correctly on those grids. Various schemes have been proposed to improve this, both for finite volume [*Auth and Harder*, 1999; *Trompert and Hansen*, 1996] and finite element discretizations [*Moresi and Solomatov*, 1995; *Yang and Baumgardner*, 2000]. In STAG3D a major improvement was obtained by relaxing the momentum and continuity equations simultaneously for each cell (consisting of a central pressure point and six surrounding staggered velocity points) using a matrix solver, rather than using separate iteration sweeps for the x momentum, y momentum, z momentum, and continuity equations as done previously [*Tackley*, 1993]. An additional improvement was obtained by using extra iterative sweeps in the upper 0.2 of the box, where the largest viscosity gradients occur (instead of the whole box). However, despite these improvements the code is still not as robust as desired, and viscosity variations must be limited through the viscosity law and viscosity cutoffs.

[20] The inclusion of nonlinear rheology requires iterations at each time step between the (velocity, pressure) solution and the effective viscosity field, in order to obtain mutually consistent viscosity and velocity fields. Although this may require tens of iterations when calculating the initial solution, in subsequent time stepping the solution changes slowly, and only one or two outer iterations are usually required at each time step.

[21] STAG3D is designed to run on parallel computers, and the presented calculations were run on eight CPUs each of a cluster

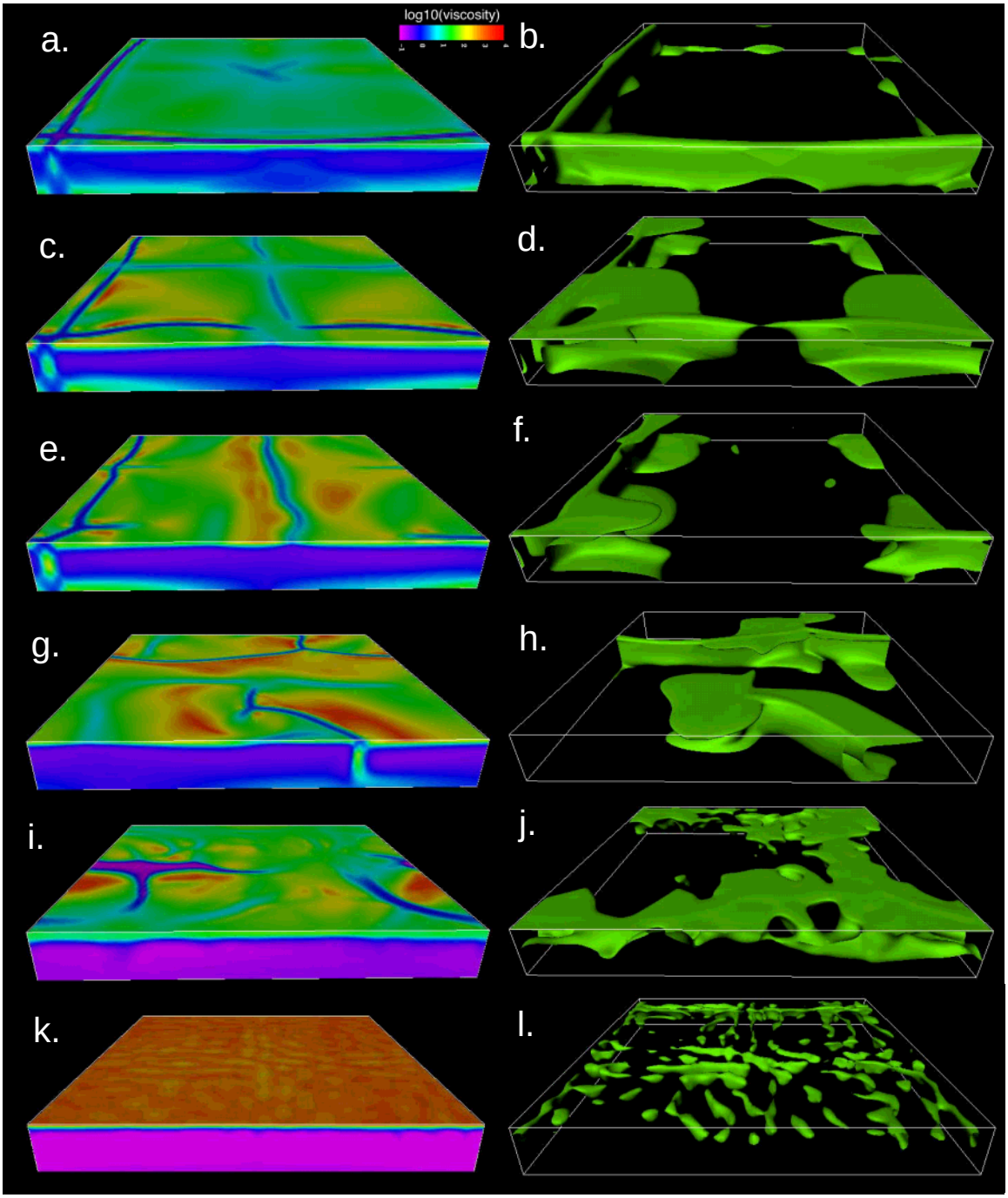

Figure 3. Viscosity fields (left column) and temperature isosurfaces (right column) for selected cases with constant yield stress (Figures 3a and 3b) 2.8×10^3, (Figures 3c and 3d) 5.7×10^3, (Figures 3e and 3f) 7.1×10^3, (Figures 3g and 3h) 8.5×10^3, (Figures 3i and 3j) 1.4×10^4, and (Figures 3k and 3l) 2.8×10^4. The color bar shows log10(viscosity), which varies between 0.1 and 10,000. The horizontal viscosity slice is at $z = 0.97$. Isosurfaces show where the temperature is 0.1 lower than the geotherm.

of 24 dual-400MHz processor Pentium II PCs with the Linux operating system and MPI for message passing. For this study a large number of cases were desired, leading to a choice of resolution and hence convective vigor (Rayleigh number) somewhat less than state of the art (this highlights a common dilemma in numerical simulation: between running a small number of "leading-edge" cases or a large number of more routine cases). A resolution of 128 × 128 × 32 cells was chosen, with convective parameters Ra_T = 10^5 and H = 10 (equal to the time-averaged surface heat flow), hence Ra_H = 10^6. With the rheologies used, internal temperatures were typically of order 1.0, implying an upper thermal boundary layer of thickness order 0.1, which together with vertical grid refinement in the upper boundary layer gave at least 5 vertical cells over the lithosphere. Since downwellings are generally double-sided, they are at least twice as wide as the upper boundary layer thickness, so higher horizontal grid spacing is appropriate. Resolution tests, in which calculations were performed on grids ranging from much coarser to twice as fine in each direction, are presented in the second paper (part 2).

2.5. Diagnostics of Platelike Behavior

[22] It is desirable to define some quantitative measures of platelike behavior to apply to analyzing the results, rather than relying solely on visual impressions. The criteria chosen here are "plateness" (the degree to which surface deformation is localized), "mobility" (the extent to which the lithosphere is able to move), and toroidal:poloidal ratio. A similar set of three diagnostics was defined by *Zhong et al.* [1998] on the basis of a prescribed geometry; here, different definitions are developed for the freely convecting system. These are discussed and rigorously defined below. Of course, there are other characteristics of plate tectonics that are also desirable, but for which it is difficult to define quantitative measures. For example, plate boundaries should perhaps come in three distinct types: symmetric spreading centers, single-sided subduction zones, and transform faults. The time evolution of the plates should bear a resemblance to that of Earth's plates [*Scotese*, 1991], including, for example, sudden changes in plate motion and jumps in plate boundaries [*Bonatti et al.*, 1994].

2.5.1. Plateness

[23] Perhaps the most fundamental characteristic of plate tectonics is that of almost rigid plates separated by weak boundary regions in which the vast majority of the deformation occurs. The first quantitative measure of this was defined by *Weinstein and Olson* [1992] for 2-D calculations (i.e., with a one-dimensional surface). In three dimensions it is necessary to define a new plateness suitable for analyzing two-dimensional surface deformation. The definition used here is based on the principle that most of the surface deformation (strain rate) should occur in a small fraction of the surface area. Specifically, the square root of the second invariant of two-dimensional strain rate

$$\dot{\varepsilon}_{\mathrm{surf}} = \sqrt{\dot{\varepsilon}_{xx}^2 + \dot{\varepsilon}_{yy}^2 + 2\dot{\varepsilon}_{xy}^2} \qquad (10)$$

is considered. The total (integrated) $\dot{\varepsilon}_{\mathrm{surf}}$ is calculated, followed by the fraction of the surface area in which the highest 80% of that deformation occurs. This area fraction, denoted f_{80}, would be zero for perfect plates (all deformation takes place within infinitely narrow zones) and 0.8 for uniformly distributed deformation. However, even for constant-viscosity convection there is some localization of surface deformation, because regions above downwellings (and localized upwellings in basally heated cases) have higher strain rates.

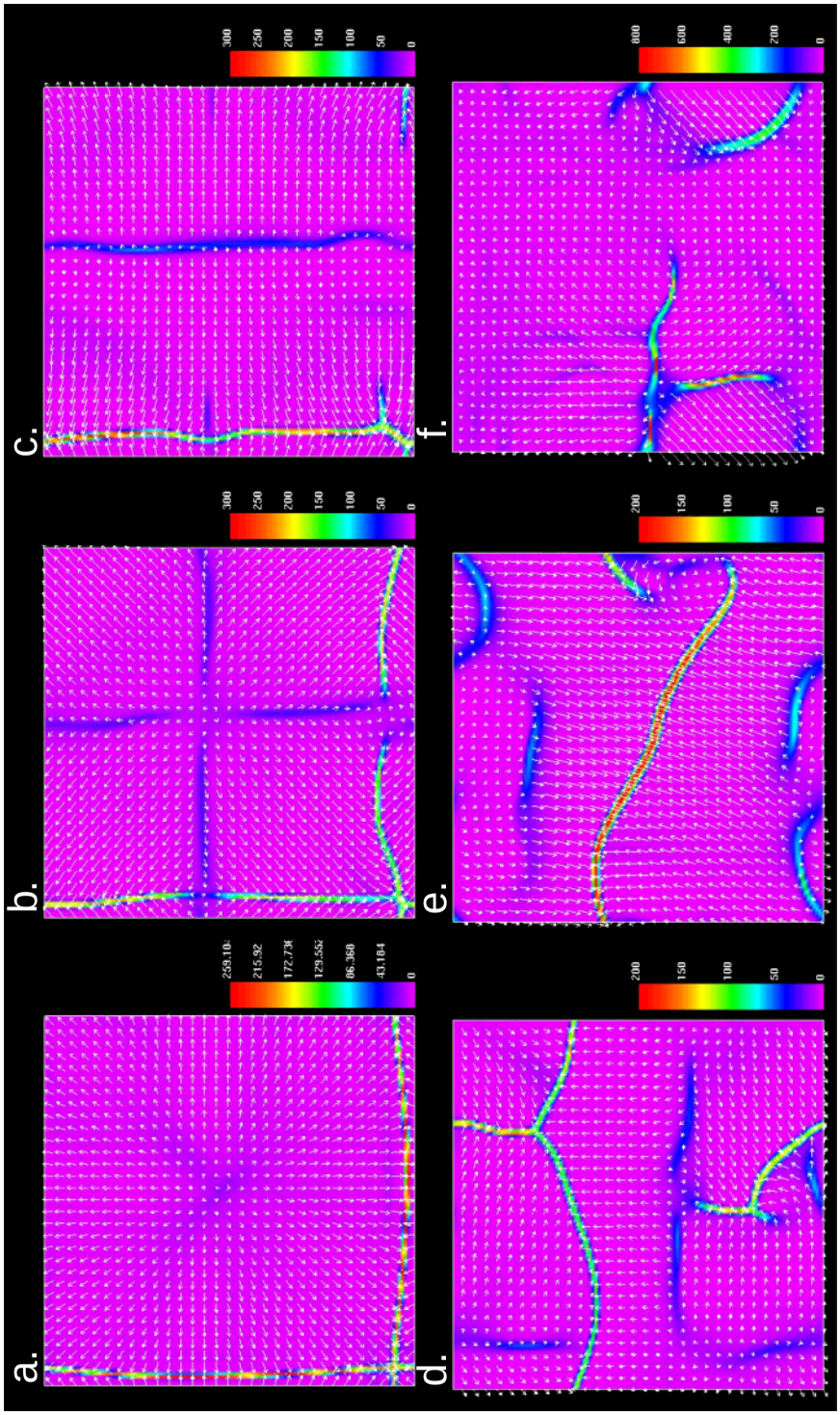
a.
b.
c.
d.
e.
f.

Internally heated calculations with $Ra_H = 10^6$ (presented later) have $f_{80} \approx 0.6$, meaning that 80% of the surface deformation occurs in 60% of the surface area. While this fraction may change with Ra and heating mode, the present study is localized to these parameters. Ideally, plateness should vary between 0 for constant-viscosity cases to 1.0 for perfect plates, thus the definition:

$$P = 1 - \frac{f_{80}}{0.6} \tag{11}$$

The possibility of negative P occurs with the above definition; physically, this corresponds to deformation which is more distributed than that of constant-viscosity convection.

[24] What is P for Earth? There is an increasing recognition that plates are not as rigid as once thought; for example, *Gordon and Stein* [1992] point out that many plate boundaries, both continental and oceanic, are hundreds to thousands of kilometers wide, with these wide plate boundary zones taking up 15% of Earth's surface area. Thus, P is certainly not 1.0, but is probably quite high. A global model of plate motion and margin widths was constructed by *Dumoulin et al.* [1998], and it would be interesting to calculate the above defined P on the basis of their model.

2.5.2. Mobility

[25] Plates should not only be rigid but also move. Here mobility is simply defined as the ratio of rms surface velocity to rms velocity averaged over the entire 3-D domain:

$$M = \frac{(v_{\mathrm{rms}})_{\mathrm{surface}}}{(v_{\mathrm{rms}})_{\mathrm{whole}}} \tag{12}$$

[26] For constant-viscosity, internally heated convection, $M \approx 1$. For the internally heated, platelike cases discussed later, M is in the range 1.2–1.3. For rigid-lid cases, M is very small.

2.5.3. Toroidal:poloidal ratio

[27] Any three-dimensional velocity field can be divided into poloidal and toroidal components. Poloidal flow is associated with divergence or convergence in a horizontal plane, i.e., spreading centers and subduction zones, while toroidal flow is associated with vertical vorticity (rotation in the horizontal plane) generated by transform (strike-slip) motion or plate rotation. The velocity field of Earth's surface has a toroidal component which is a substantial fraction of the poloidal flow [*Hager and O'Connell*, 1978]. Although the term "equipartitioning" is often used, the toroidal component is actually somewhat smaller than the poloidal component, with the amplitude ratio varying between about 0.25 and 0.5 (excluding net rotation) in the last 120 million years [*Lithgow-Bertelloni et al.*, 1993; *Olson and Bercovici*, 1991].

[28] Such a large toroidal component is curious because toroidal motion is not driven directly by mantle buoyancy forces, and variable viscosity convection calculations typically exhibit only a small toroidal:poloidal energy ratio, of order a few percent [*Balachandar et al.*, 1995; *Christensen and Harder*, 1991]. It is thought that the large toroidal flow is caused by the coupling of mantle buoyancy sources with the plates [*Gable et al.*, 1991], and thus toroidal:poloidal ratio is often cited as an important characteristic of plate beha-

Figure 4. Surface strain rate fields and velocities for selected cases with constant yield stresses of (a) 2.8×10^3, (b) 5.7×10^3, (c) 7.1×10^3, (d) 8.5×10^3, (e) 9.9×10^3, and (f) 1.4×10^4. The color bars show relative units. Instantaneous diagnostics are (a) $R_{\mathrm{TP}} = 0.03$, $P = 0.34$; (b) $R_{\mathrm{TP}} = 0.11$, $P = 0.60$; (c) $R_{\mathrm{TP}} = 0.14$, $P = 0.63$; (d) $R_{\mathrm{TP}} = 0.31$, $P = 0.66$; (e) $R_{\mathrm{TP}} = 0.43$, $P = 0.74$; and (f) $R_{\mathrm{TP}} = 0.37$, $P = 0.43$.

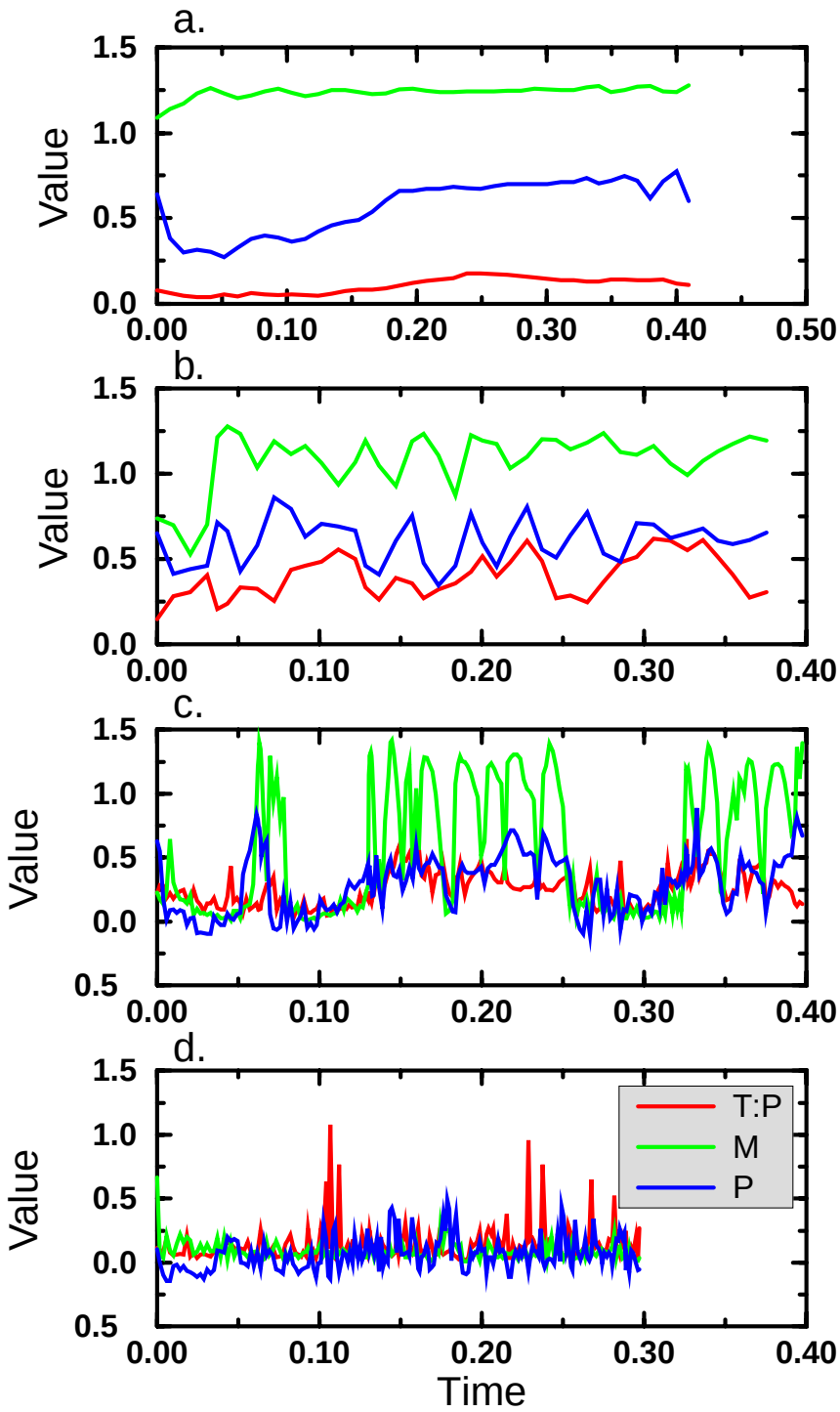

Figure 5. Time series of plate diagnostics (red) surface toroidal:poloidal ratio, (green) surface mobility, and (blue) plateness for selected cases with constant yield stress values (a) 5.7×10^3, (b) 8.5×10^3, (c) 1.4×10^3, and (d) 2.8×10^4.

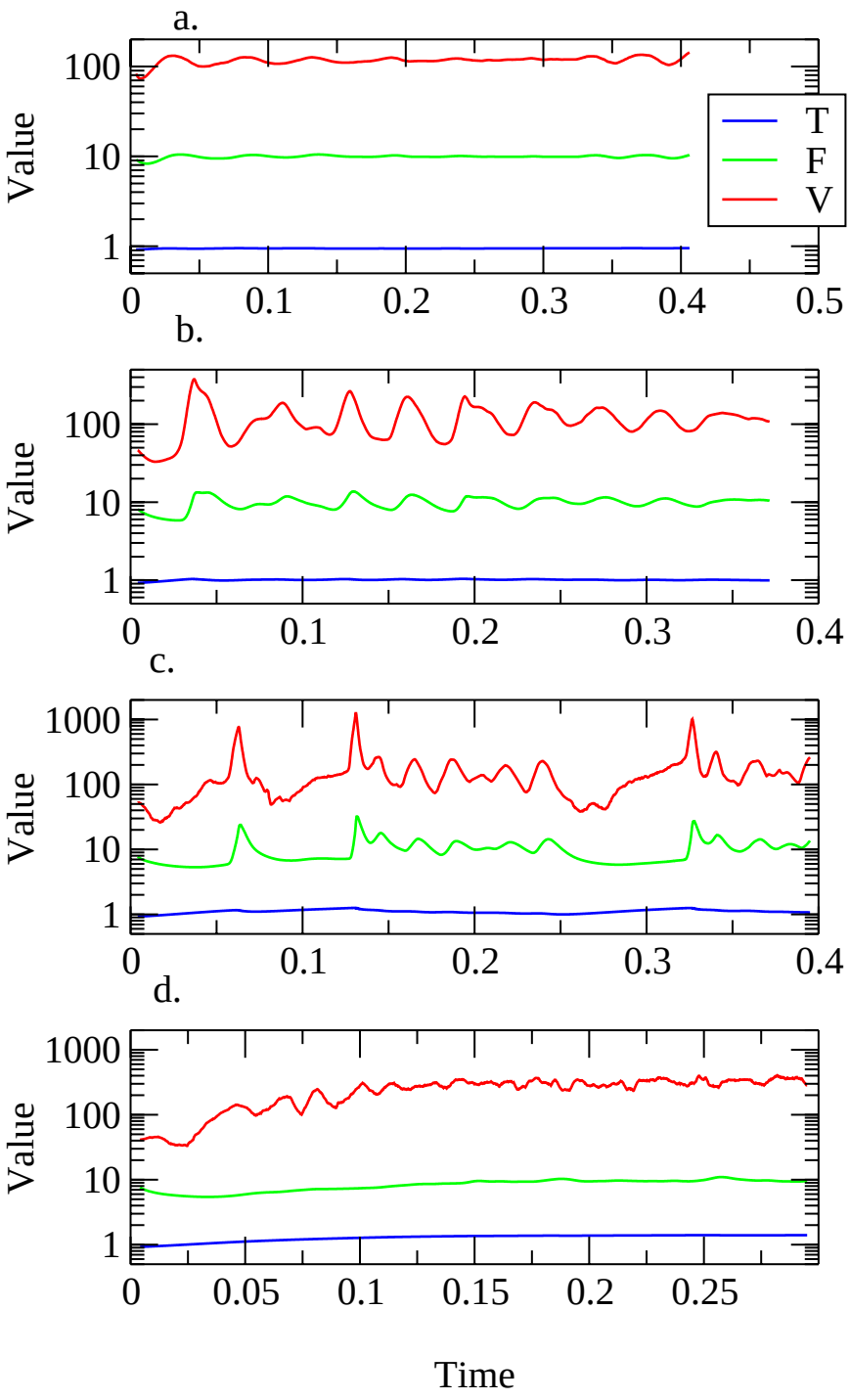

Figure 6. Time series of surface heat flux F, volume-averaged rms velocity, and volume-averaged temperature for selected cases with constant yield stress values (a) 5.7×10^3, (b) 8.5×10^3, (c) 1.4×10^4, and (d) 2.8×10^4.

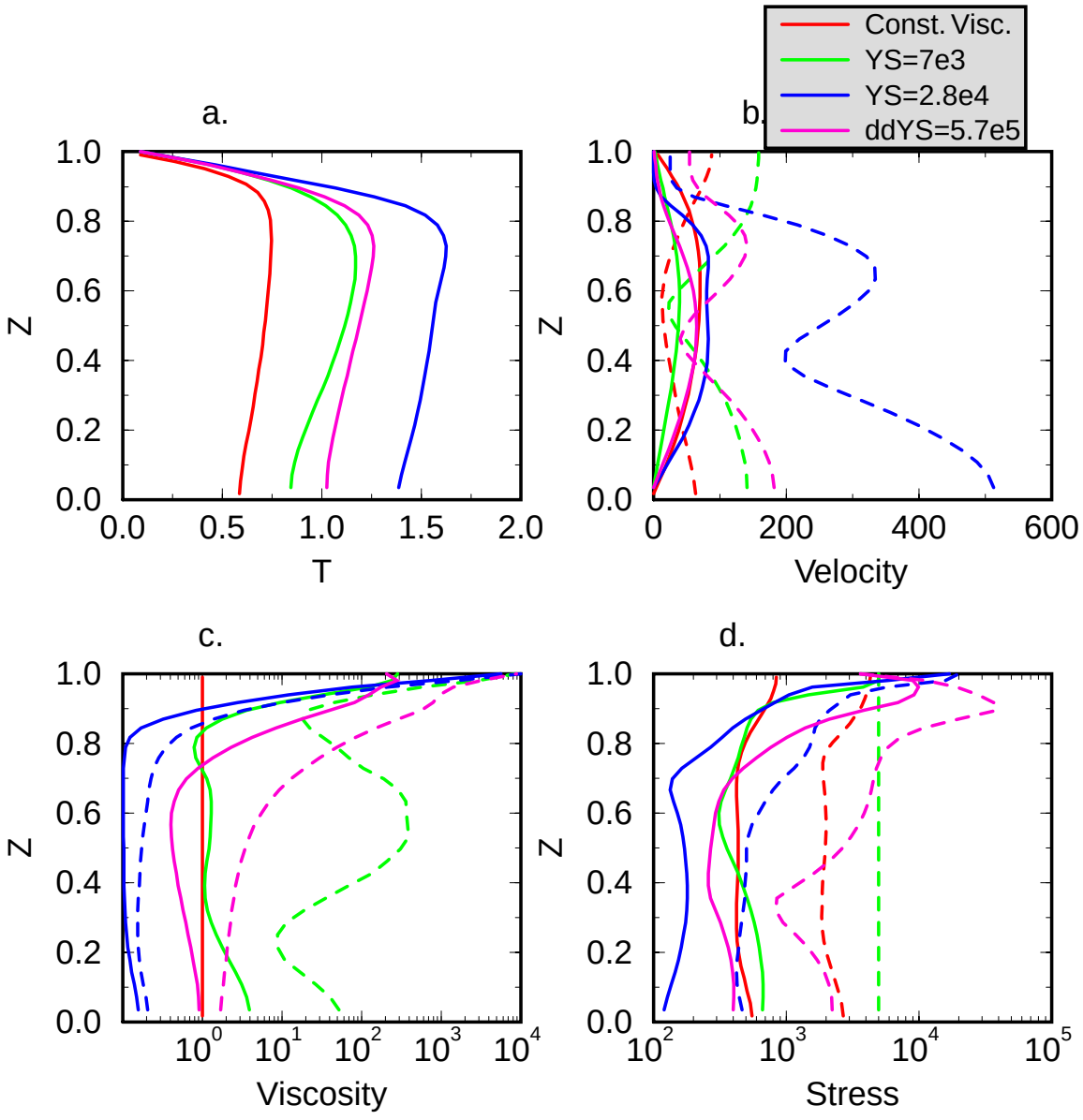

Figure 7. Radial profiles of horizontally averaged quantities for constant-viscosity convection (red), two cases with constant yield stress value 7.1×10^3 (green) and 2.8×10^4 (blue), and a case with depth-proportional yield stress gradient 5.7×10^5: (a) temperature, (b) velocity: horizontal (solid lines) and vertical (dotted lines), (c) viscosity (solid lines) and maximum viscosity (dotted lines), and (d) rms stress (solid lines) and maximum stress (dotted lines).

vior. However, it does not seem to be an essential characteristic since it is possible to imagine plate tectonics with small toroidal motion, particularly in Cartesian geometry, where the system could evolve into a system of rolls. Even so, the toroidal:poloidal ratio is of great interest and so is calculated for these 3-D models.

[29] Since STAG3D works with total velocity (unlike spectral methods, which commonly use toroidal and poloidal potentials), some effort is required to decompose the velocity field into toroidal and poloidal components. This decomposition is performed on individual horizontal planes (e.g., the surface). To do this, the two-dimensional velocity field $\underline{v}_h$ is expressed as the sum of poloidal ($\underline{v}_{h,\mathrm{pol}}$) and toroidal ($\underline{v}_{h,\mathrm{tor}}$) terms, each of which can be derived from a two-dimensional scalar, ϕ and ψ, respectively:

$$\underline{v}_h \equiv \underline{v}_{h,\mathrm{pol}} + \underline{v}_{h,\mathrm{tor}} \equiv \underline{\nabla}_h \varphi + \underline{\nabla} \times (\psi \hat{z}), \qquad (13)$$

where $\underline{\nabla}_h$ is the horizontal gradient operator and $\underline{\hat{z}}$ is a vertical unit vector. Taking the horizontal divergence of this yields a simple Poisson equation for the poloidal velocity potential, and taking the vertical vorticity yields a Poisson equation for the toroidal velocity scalar:

$$\nabla^2 \varphi = \underline{\nabla}_h \bullet \underline{v}_h; \nabla^2 \psi = \mathrm{vort}_z(\underline{v}_h). \qquad (14)$$

[30] A simple multigrid Poisson solver is then used to obtain ϕ and ψ, from which the toroidal and poloidal horizontal velocity components are calculated. For 3-D fields the vertical velocity component v_z is added to the poloidal field. The toroidal:poloidal ratio is simply

$$R_{TP} = \sqrt{\frac{\langle v_{\mathrm{tor}}^2 \rangle}{\langle v_{\mathrm{pol}}^2 \rangle}}, \qquad (15)$$

where, in the presented results, the mean is taken over the top surface of the domain. This decomposition process is compiled as a module in the 3-D visualization package IRIS Explorer, allowing instant visualization of the toroidal and poloidal fields. The correctness of the decomposition was verified by checking that calculated toroidal and poloidal components added up to the original velocity field, that the calculated poloidal field had zero vertical vorticity, and that the calculated toroidal field had zero horizontal divergence. Application of this decomposition to constant-viscosity results (which ideally have zero toroidal flow) yielded very small toroidal:poloidal ratios of order 10^{-4}–10^{-5}), consistent with the accuracy of single-precision arithmetic, indicating that significant (e.g., of order 10^{-2}–10^{-1}) toroidal flow, when found, is not an artifact of numerical leakage.

3. Results

3.1. Cases, Parameters, and Scalings

[31] As mentioned earlier, cases are performed in an 8 × 8 × 1 Cartesian box with free-slip horizontal boundaries and periodic sides. The upper boundary is isothermal, and the lower boundary is zero heat flux. The default thermal parameters are $Ra_T = 10^5$ and $H = 10$ ($Ra_H = 10^6$), and the default viscosity parameters were given in an earlier section.

3.1.1. Three series

[32] As discussed earlier, the most realistic form of lithospheric strength profile is thought to be proportional to depth near the surface ("brittle" deformation) and approximately constant at greater depth ("ductile" deformation). However, for the sake of understanding the influence of each component, the idealized cases of constant yield stress and depth-proportional yield stress are considered first, followed by the more realistic composite yield stress. Thus there are three series of cases: (1) constant yield stress, (2) depth-proportional yield stress, and

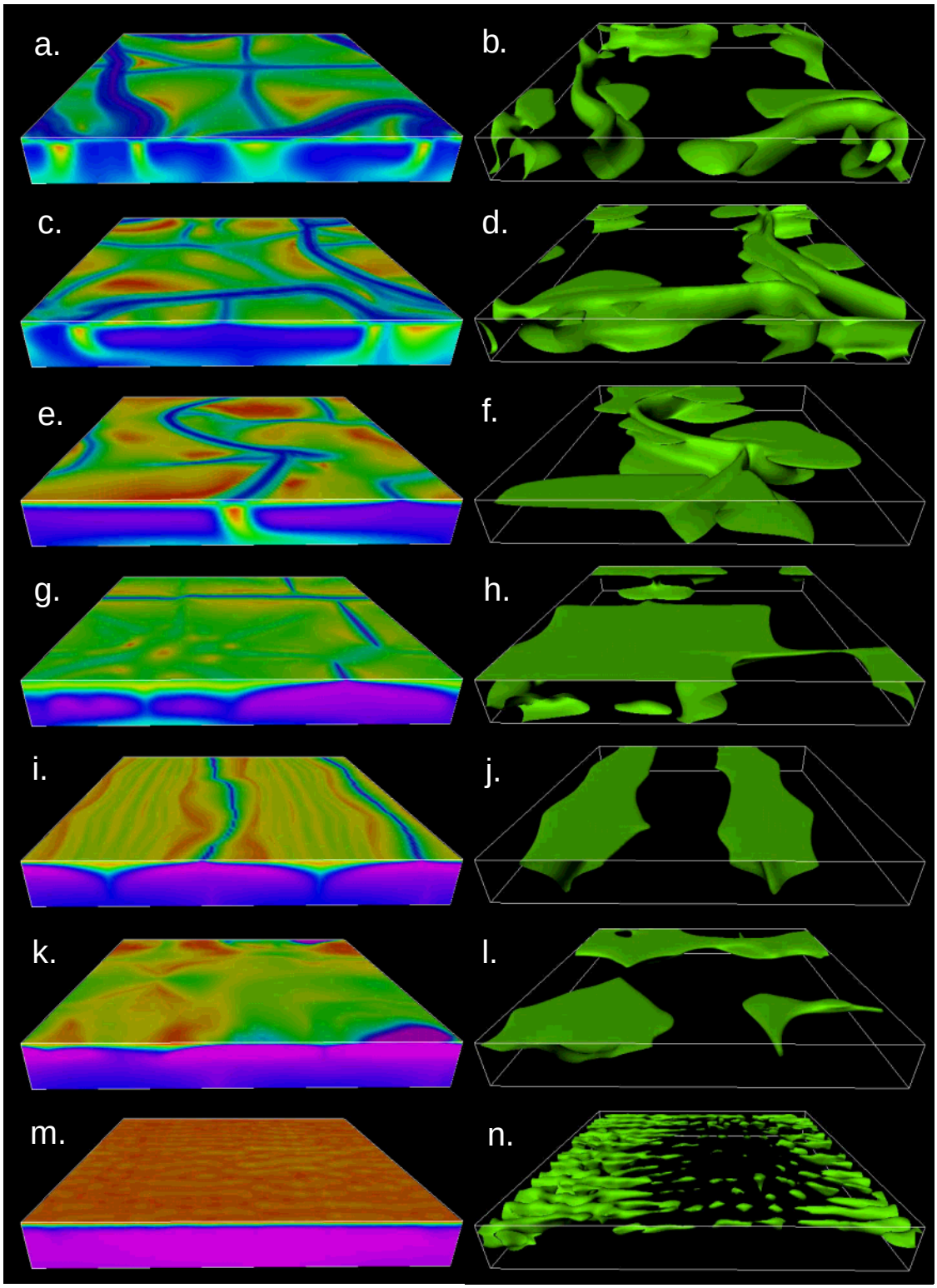
a.
b.
c.
d.
e.
f.
g.
h.
i.
j.
k.
l.
m.
n.

(3) composite yield stress. The values of these yield stresses are not fixed at the values in Figure 1 but rather are varied over a wide range, which is reasonable owing to uncertainties in actual fault strength and effective lithospheric strength, as discussed earlier.

3.1.2. Composite yield stress

[33] In the cases with both brittle and ductile yield stress included, there are obviously a large number of possible combinations of σ_y and σ_y', too many to run for one study. Here it was decided to stick to cases where $\sigma_y' = 20\sigma_y$, meaning that the upper 1/20th of the box (nominally 1/2 the upper boundary-layer thickness) experiences the depth-proportional brittle yield stress, with the rest of the box experiencing the constant ductile yield stress. While, from previous discussion, this may seem to be a rather deep intersection, the heat flux in these models is a factor of 5 lower than that of Earth (as discussed later), meaning that the upper boundary layer is 5 times too thick, and if the intersection depth were scaled by this amount, it would correspond to a brittle-ductile transition depth of $\sim$30 km. In any case, these "composite" yield stress models display some distinctly different characteristics from those with only one or the other type included.

3.1.3. Dimensional scaling

[34] How should the nondimensional input parameters and output variables in these results, which are at relatively low heat flux and convective vigor, be scaled to dimensional values appropriate for Earth? Table 1 gives a reasonable (though not unique) set of dimensional scalings, starting with assumed parameter values, then listing derived quantities, with scalings given for both unit and interesting values. It is chosen to assume realistic (for the uppermost mantle) physical parameter values except for the reference viscosity, which is at least 2 orders of magnitude too high. The temperature scale ΔT is the temperature drop over the upper boundary layer (lithosphere), since the lower boundary layer is not included. With these assumptions, Earth's heat flux of $\sim$80 mW/m^2 corresponds to $\sim$50 nondimensional units, so the modeled flux of 10 is a factor of 5 too low. For stresses and stress gradients, the second or third scalings are given to allow easy conversion of the input yield stresses. In Figure 1 (and *Kohlstedt et al.* [1995]), the strength of the midlithosphere is about 700 MPa, while the brittle strength gradient is around 70 MPa/km. To interpret nondimensional velocities in terms of Earth equivalents, it may be reasonable to assume that velocity scales as (heat flux)^2, as simple boundary-layer theory predicts [*Turcotte and Schubert*, 1982], leading to a predicted increase of factor 25. Thus, for example, 100 nondimensional velocity units might scale to 2.5 cm/yr. One nondimensional time unit would scale to 265 billion years, or 10.6 billion years if reduced by the predicted increase in velocities. Cases were run for nondimensional (i.e., thermal diffusion) times of $\sim$0.4, corresponding to scaled times of $\sim$4 billion years.

Figure 8. Viscosity fields (left column) and temperature isosurfaces (right column) for selected depth-proportional yield stress cases. The color bar shows log10(viscosity), which varies between 0.1 and 10,000. The horizontal viscosity slice is at $z = 0.97$. Isosurfaces show where the temperature is 0.1 lower than the geotherm. Yield stress gradients are (Figures 8a and 8b) 8.5×10^4, (Figures 8c and 8d) 1.4×10^5, (Figures 8e and 8f) 2.0×10^5, (Figures 8g and 8h) 2.8×10^5, (Figures 8i and 8j) 5.7×10^5, (Figures 8k and 8l) 1.1×10^6, and (Figures 8m and 8n) 1.7×10^6. A new convective mode, with focused spreading centers but distributed downwellings, is displayed in Figures 8i and 8j.

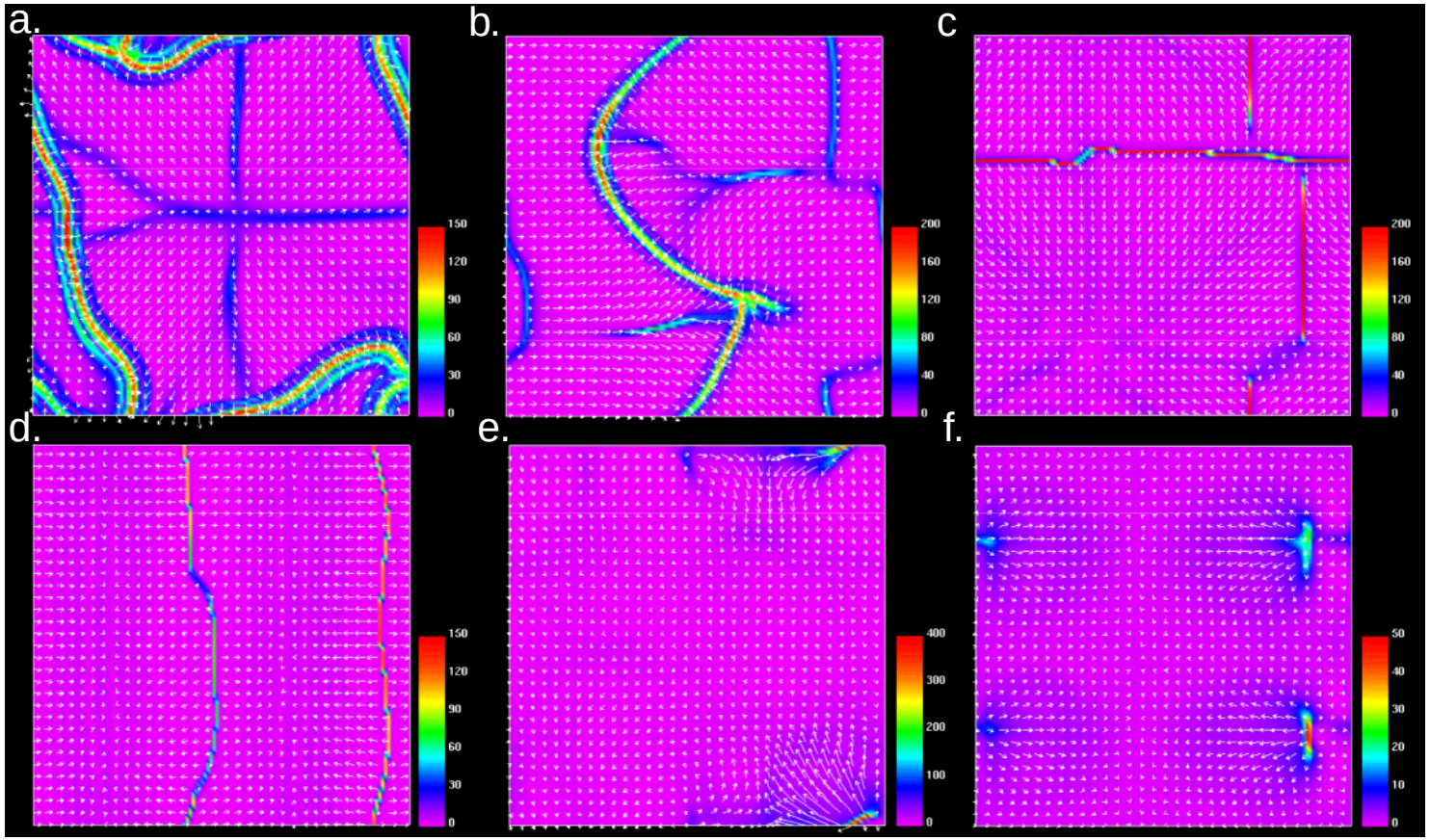

Figure 9. Surface strain rate fields for selected cases with depth-proportional yield stress with gradients of (a) 8.5×10^4, (b) 2.0×10^5, (c) 2.8×10^5, (d) 5.7×10^5, (e) 1.1×10^6, and (f) 1.1×10^6. Color bars show relative units. Instantaneous diagnostics are (a) $R_{TP} = 0.29$, $P = 0.61$; (b) $R_{TP} = 0.43$, $P = 0.74$; (c) $R_{TP} = 0.21$, $P = 0.30$; (d) $R_{TP} = 0.19$, $P = 0.39$; (e) $R_{TP} = 0.86$, $P = 0.41$; and (f) $R_{TP} = 0.34$, $P = 0.054$.

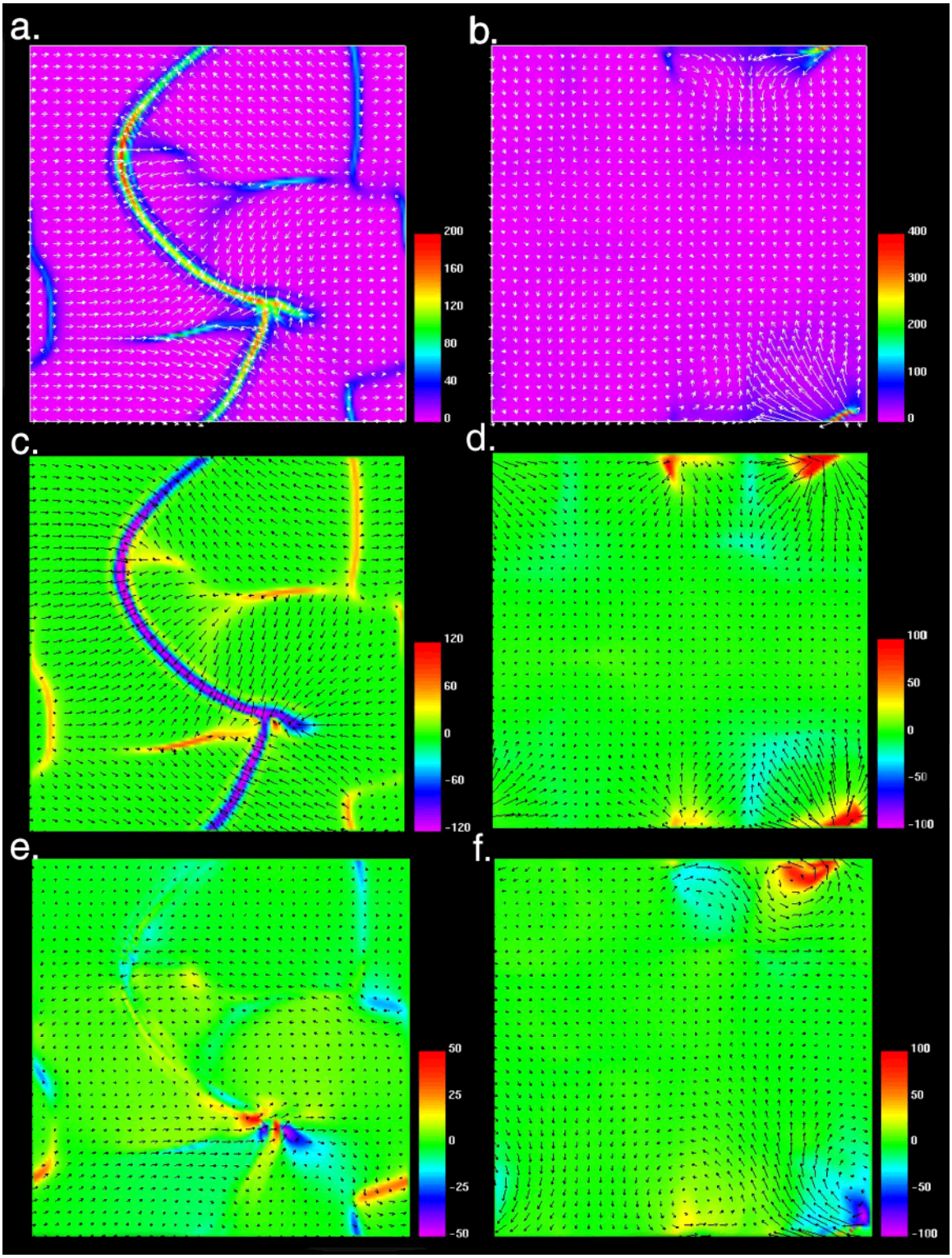
a.
200
160
120
80
40
0
b.
400
300
200
100
0
c.
120
60
0
-60
-120
d.
100
50
0
-50
-100
e.
50
25
0
-25
-50
f.
100
50
0
-50
-100

3.2. Constant-Viscosity Convection

[35] It is useful to start by considering the surface deformation associated with constant-viscosity convection. Figure 2 shows the surface deformation, velocity, and 3-D temperature distribution for a constant-viscosity case with the standard parameters ($Ra_T = 10^5$, $H = 10$). As usual [*Bercovici et al.*, 1989; *Houseman*, 1988; *Parmentier et al.*, 1994; *Travis et al.*, 1990], the temperature field is characterized by closely spaced, time-dependent cylindrical downwellings. The surface strain rate is high above these downwellings but rather low elsewhere, indicating that even constant-viscosity convection displays some localization of surface deformation. Globally averaged quantities (not shown here for space reasons) are only weakly time dependent. Surface mobility is always close to 1.0, while plateness stays close to zero. Depth profiles of various quantities are discussed later.

3.3. Constant "Ductile" Yield Stress

[36] Cases with temperature-dependent viscosity were run for eight different values of constant yield stress, ranging from 2.8×10^3 to 2.8×10^4 (34–340 MPa, all less than the "experimental" value of ~700 MPa in Figure 1), which encompasses a large range in system behavior. The viscosity and temperature structures of six of these cases are illustrated in Figure 3, with yield stress increasing from top to bottom. The lower yield stress (σ_y) cases have mobile, smoothly evolving upper boundary layers (top three rows), while the highest σ_y case (bottom) is in the rigid-lid mode, and the intermediate cases have erratic, time-dependent lid mobility.

3.3.1. Planform

[37] The temperature fields of the cases with mobile lids are completely different from that of the constant-viscosity case (Figure 2b), being characterized by long linear downwellings with a spacing as large as that allowed by the box size. The rigid-lid case (Figure 3f) displays closely spaced downwellings, which, however, do not look like the usual downwellings in rigid-lid convection [e.g., *Tackley*, 1993]; this is because there is still some limited lid deformation, which allows some long-wavelength flow to be set up.

3.3.2. Viscosity

[38] The viscosity fields span 5 orders of magnitude, and platelike behavior, where present, is indicated by strong (green to red) plates surrounded by narrow weak (blue to purple) zones. At a low yield stress (Figure 3a), focused weak zones are formed above the linear downwellings, but divergent regions are diffuse, with significant distributed deformation, and the lithosphere is fairly weak. The effective viscosity in the lithosphere is determined by yielding, rather than the intrinsic temperature dependence of viscosity. As σ_y is increased, the divergent zones become increasingly localized, and the plates become stronger, as illustrated in Figures 3c and 3e, where the behavior is the most "platelike" of this series, with a network of localized passive spreading centers and "subduction" zones. The higher yield stress in Figure 3e results in an almost

Figure 10. Decomposition of surface velocity field into toroidal and poloidal components for two cases with depth-proportional yield stress: (Figures 10a, 10c, and 10e) yield stress gradient 2.0×10^5 and (Figures 10b, 10d, and 10f) yield stress gradient 1.1×10^6. The top row (Figures 10a and 10b) shows total surface velocity field and surface strain rate. The middle row (Figures 10c and 10d) shows poloidal velocity field and horizontal divergence. The bottom row (Figures 10e and 10f) shows toroidal velocity field and vertical vorticity.

two-dimensional flow pattern. Downwellings are generally double-sided, with a broad shallow weak zone making a transition to a deeper conjugate pair of narrow weak zones inclined at $\sim 45^{\circ}$. No purely strike-slip boundaries are formed.

[39] At slightly higher σ_y (Figure 3g), plate boundaries are incomplete, i.e., they do not form a complete interconnected network, and the system becomes increasingly time dependent (as explored in later figures). At the σ_y value of Figure 3i, there are periods of immobile lid as well as periods of very vigorous lid mobility.

[40] At the highest σ_y (Figure 3e), an immobile lid is formed, and the interior temperature is much higher (as indicated by its lower viscosity). In this mode, only a temperature variation of order the rheological temperature scale participates in convection [*Moresi and Solomatov*, 1995], and the system heats up until convection with this temperature variation is vigorous enough to transport the specified internal heating of 10 to the base of the rigid lid. Because the model viscosity variation with temperature is lower than realistic, (1) a larger than realistic ΔT will participate in the convection and (2) the interior temperature needs to increase by a larger amount to obtain low viscosities needed for more vigorous convection. If the cases were basally heated, rather than internally heated, the temperature rise would also be less and the surface heat flux would decrease instead.

[41] Although the yield stress criterion is applied at all depths, in general, it has a large effect only in the lithosphere, because this is where stress levels are highest. This can be seen in the viscosity field cross sections in Figure 3, where downwellings are high viscosity below the weak plate boundary. However, deeper yielding may also be observed, for example, where the cold downwellings reach the base of the mantle. This is probably an unrealistic result of using such an idealized rheology, although the presence of large earthquakes >600 km deep in subduction zones indicates that slow viscous creep is not the only deformation mechanism taking place even at substantial depth. It is probable that in reality the "ductile" yield stress should increase with depth.

3.3.3. Surface deformation

[42] The transitions in surface deformation style in the mobile-lid regime are more clearly visible in Figure 4, which shows typical surface deformation fields as σ_y is increased from 2.8×10^3 (34 MPa) to 1.4×10^4 (168 MPa). A gradual sharpening-up of passive spreading centers is seen with increasing σ_y up to 7.1×10^3 (85 MPa) (Figures 4a–4c), followed by a transition from continuous smoothly evolving plates to erratic platelike behavior (Figures 4d–4f). This erratic regime is characterized by highly time-dependent localized convergent and divergent zones which form an incomplete network of plate boundaries; that is, the plate boundary zones do not form an interconnecting network as at slightly lower σ_y values. The frames illustrated in Figures 4d–4f are chosen to be representative of this mode of behavior, although there are large variations. Increasing σ_y results in greater time dependence and spatial variability; for example, Figure 4f shows a frame in which only a small part of the lid is moving. The "gaps" in the global plate boundary network are filled by broad deformation zones, visible particularly in Figure 4f. Instantaneous surface toroidal:poloidal ratios for the illustrated frames (listed in the caption) are fairly low (0.03–0.14) for the continuously evolving mobile-lid cases (Figures 4a–4c) but Earth-like (0.3–0.43) as the surface planform becomes more erratic and less symmetric (Figures 4d–4f). Plateness increases

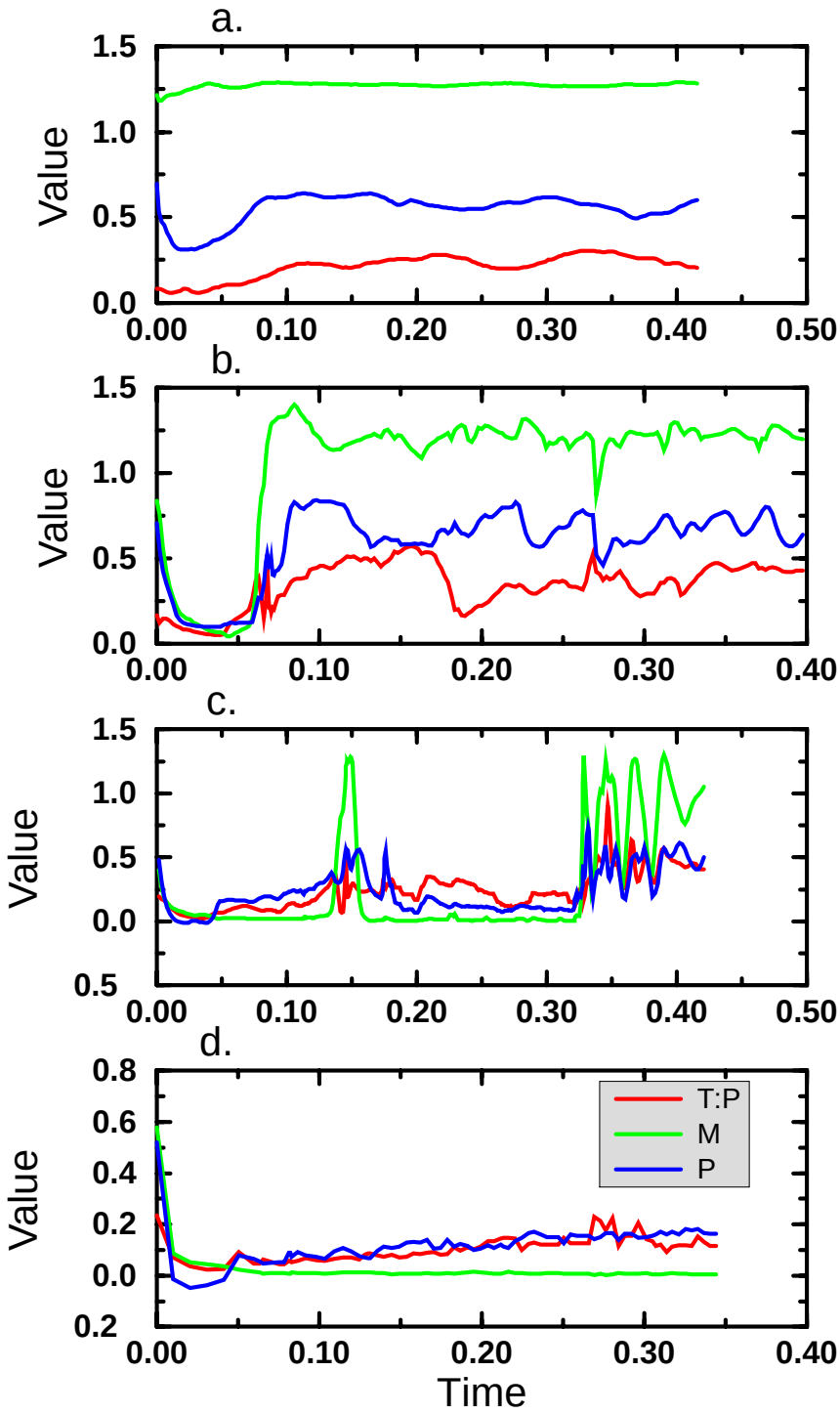

Figure 11. Time series of plate diagnostics: (red) surface toroidal:poloidal ratio, (green) surface mobility, and (blue) plateness for selected cases with depth-proportional yield stress with gradients (a) 1.4×10^5, (b) 5.7×10^5, (c) 1.1×10^6, and (d) 1.7×10^6.

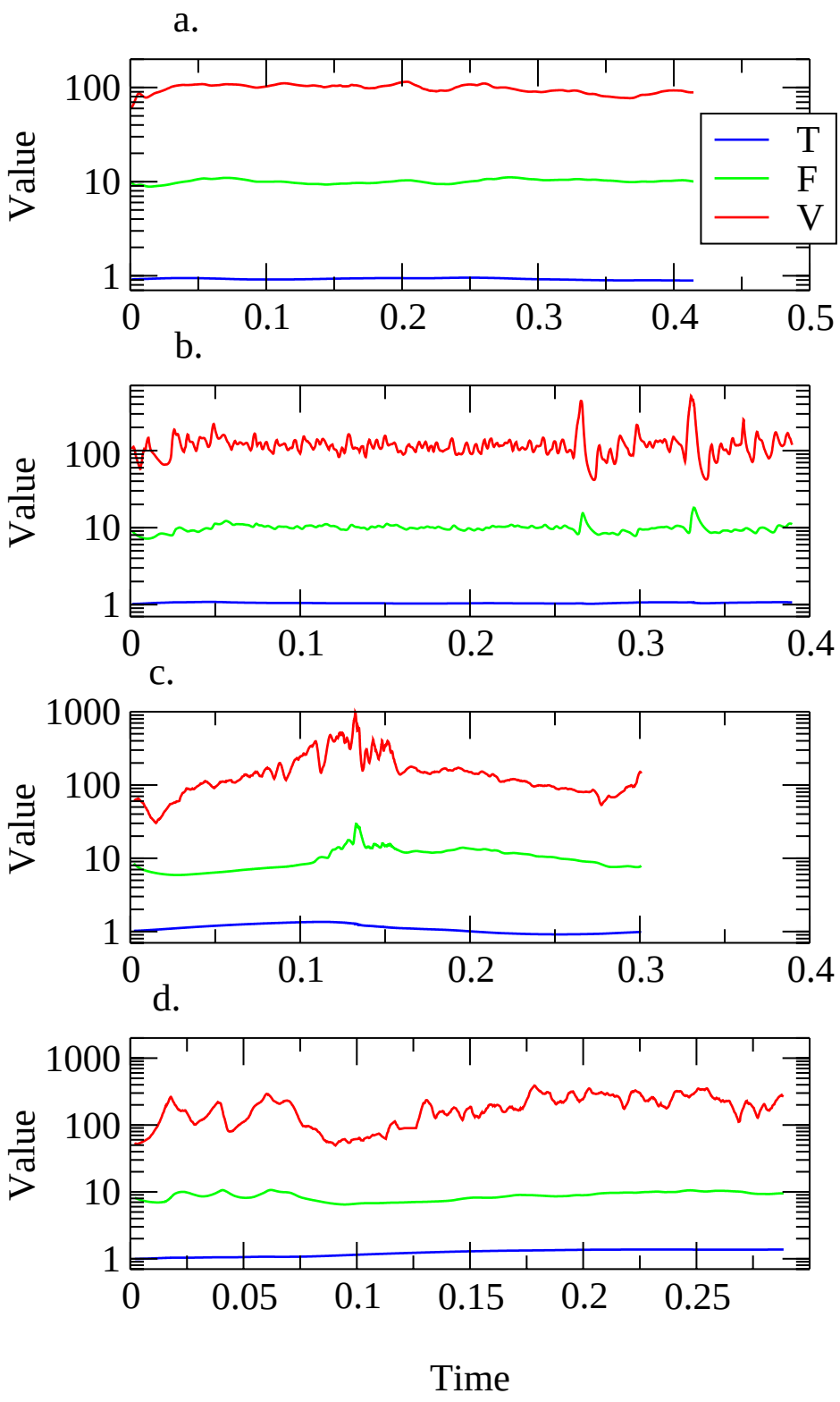
a.
b.
c.
d.
Value
100
10
1
1000
0
0.1
0.2
0.3
0.4
0.5
0.05
0.15
0.25
T
F
V
Time

with σ_y (up to 0.73 in Figure 4e) but then decreases sharply as the deformation becomes highly erratic.

3.3.4. Time dependence

[43] Time dependence of the surface deformation of the system is displayed in Figure 5, which shows R_{TP}, M, and P versus time for four yield stress values. In the continuous plates regime, time dependence is seen to increase markedly as σ_y is increased from 5.7 $\times$ 10^3 (68 MPa) to 8.5 $\times$ 10^3 (102 MPa) (Figures 5a and 5b, for the same cases shown in Figures 4b and 4d). Mobility is typically around 1.2–1.3 for both of these cases, while R_{TP} increases markedly with σ_y (peaking at values >0.5), and P shows a moderate increase. At higher σ_y (Figure 5c, corresponding to the case shown in Figure 4f), the system oscillates between periods of immobile lid (indicated by low mobility) and bursts of mobility. Even during "mobile" periods, the evolution is not smooth but seems oscillatory. The three plate diagnostics follow each other; that is, higher mobility leads to higher plateness and toroidal:poloidal ratio. For the highest σ_y (Figure 5d), the lid is always basically immobile, although clearly there is some deformation, which would likely be reduced with higher yield stresses.

[44] Time dependence of surface heat flux F, rms velocity, and mean temperature is shown in Figure 6 for the same four cases. In Figures 6a and 6b the time dependence is similar to that of the plate diagnostics in Figures 5a and 5b. In Figure 6c, dramatic bursts in heat flux and velocity accompanying transitions to platelike behavior for σ_y = 1.4 $\times$ 10^4 (168 MPa) are visible. During these transitions, velocity may peak at ~1000, 10 times its average value, and heat flow peaks at up to 30, 3 times its average value. Mean temperature rises during immobile epochs and falls during mobile-lid epochs. In the immobile lid case (Figure 6d), quantities are fairly stable, with an average rms velocity of ~300, much higher than that in mobile-lid cases.

3.3.5. Depth profiles

[45] Depth profiles of various quantities in the constant-viscosity case, the most platelike case (σ_y = 7.1 $\times$ 10^3, 85 MPa), and the immobile-lid case (σ_y = 2.8 $\times$ 10^4, 336 MPa) are shown in Figure 7. Not surprisingly, the interior temperature is slightly higher for the platelike case than for the constant-viscosity case and much higher for the rigid-lid case. Curiously, horizontal velocities are higher in the platelike case than for constant-viscosity, whereas averaged vertical velocities are lower. This is a natural consequence of the increased aspect ratio: larger aspect ratio requires higher horizontal velocities to transport the same heat, while vertical flow is focused into fewer regions, so that the average is lower. This also explains why surface mobility is higher in platelike cases than for constant-viscosity. The rms surface velocity of ~160 scales to a dimensional value (Table 1) of 0.16 cm/yr, which, when scaled to Earth convective regime, is estimated to be 3.9 cm/yr. The immobile-lid case has higher internal velocities, but the velocity does not go to zero at the surface, indicating that a higher yield stress would be needed to get a completely rigid lid.

[46] Viscosity and stress levels peak in the lithosphere, as expected [*Moresi and Soloma-*

Figure 12. Time series of surface heat flux, volume-averaged rms velocity, and volume-averaged temperature for selected cases with depth-proportional yield stress with gradients (a) 1.4 $\times$ 10^5, (b) 5.7 $\times$ 10^5, (c) 1.1 $\times$ 10^6, and (d) 1.7 $\times$ 10^6.

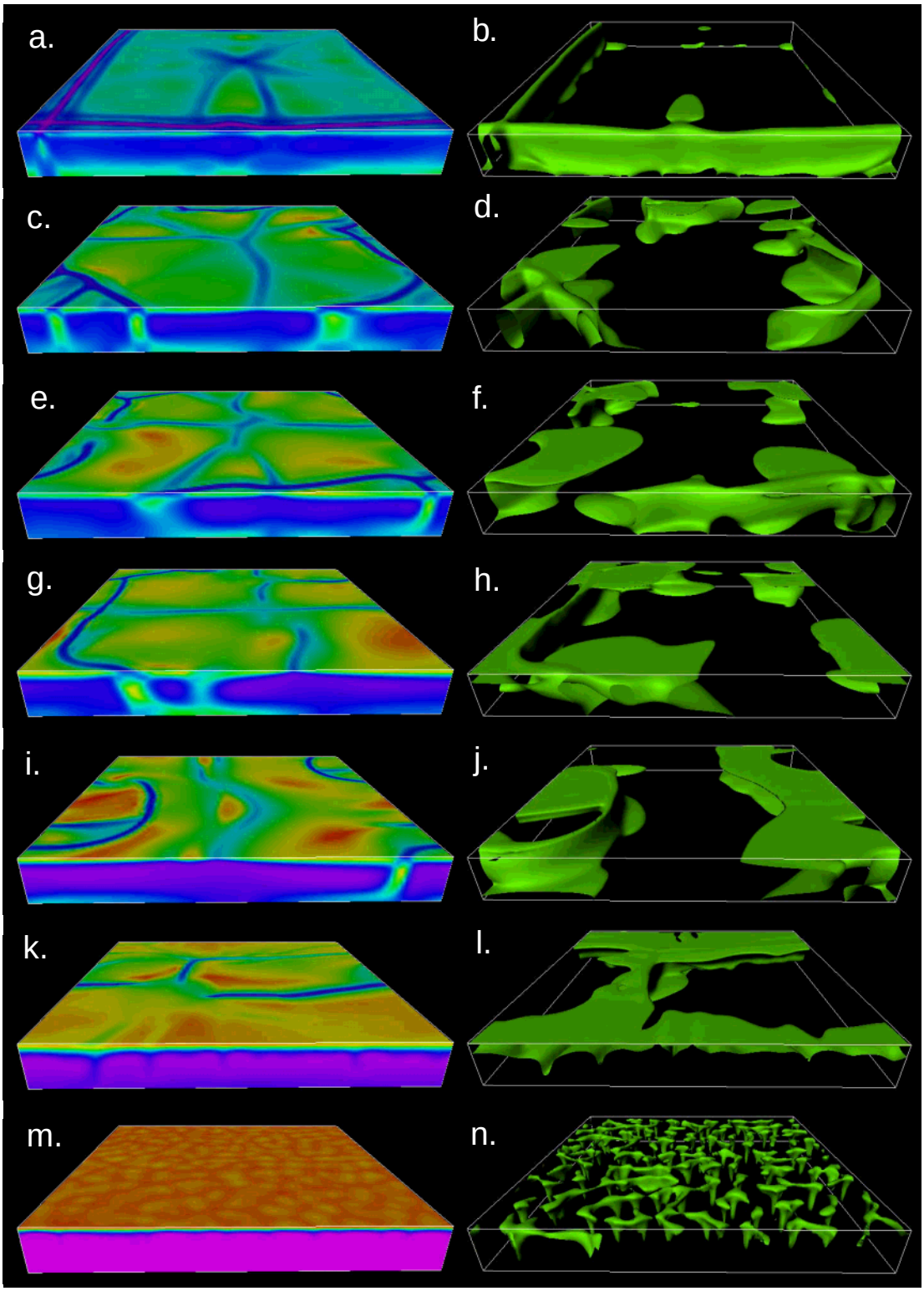
a.
b.
c.
d.
e.
f.
g.
h.
i.
j.
k.
l.
m.
n.

tov, 1995, 1998; *Tackley*, 1996a]. One interesting quantity is the "average" viscosity for the lithosphere, since global inversions for mean viscosity profile based on the geoid [e.g., *Hager and Richards*, 1989; *Ricard et al.*, 1989] obtain the best fit with a lithospheric viscosity which is only ~2 orders of magnitude higher than the upper mantle viscosity, much lower than the expected viscosity of a plate interior. In the most platelike case, the horizontally averaged lithospheric viscosity is $\sim 2 \times 10^2$, indeed about 2 orders of magnitude higher than the mean interior viscosity of around 2. From the stress profile for this case it is clear that while mean stress displays the expected decrease through the lower lithosphere, maximum stress (dotted line) is at or near the yielding limit at all mantle depths. This occurs inside the downwellings. The immobile-lid case displays lower stress levels in the interior.

3.4. Depth-Proportional "Brittle" Yield Stress

[47] Similar trends in behavior, but with some important differences, are observed in cases with a "brittle" yield stress proportional to depth. Figures 8 and 9 give a visual impression of viscosity, temperature, and surface deformation fields for different yield stress gradients σ_y' covering a range of factor 20 from 8.5×10^4 to 1.7×10^6 (1.7–35 MPa/km using the scaling in Table 1, all less than the "experimental" value in Figure 1). The best platelike behavior is observed for σ_y' toward the lower end of the considered range (Figures 8a–8d and 9a). Compared to the best constant yield stress cases, the downwellings seem to be more arcuate and migrating.

[48] The main differences to the constant yield stress cases occur for intermediate σ_y'; as this is increased, there is a gradual change from continuous to "erratic" behavior, rather than the sharper transition obtained with a constant σ_y. Weak boundary zones become more isolated, and the system becomes more time dependent.

[49] A new mode of behavior, examples of which can be seen in Figures 8g–8i and Figures 9c–9d, appears at higher σ_y'. This mode is characterized by very narrow, focused linear spreading centers but distributed downwellings and bears some resemblance (except for the focused spreading centers) to the "sluggish lid" planform obtained with intermediate temperature dependence of viscosity [*Tackley*, 1993]. Thus, in some sense, the combination of temperature dependence and pseudoplastic yielding can lead to behavior similar to moderate temperature dependence. The spreading centers are facilitated by the fact that material is very weak close to the surface. This "sluggish spreading" mode has been observed for σ_y' of up to 8.5×10^5, above which highly episodic behavior appears and eventually an immobile (but somewhat deforming) lid by σ_y' of 1.7×10^6 (35 MPa/K).

3.4.1. Toroidal and poloidal motion

[50] The instantaneous toroidal:poloidal ratios for the illustrated frames (listed in the caption

Figure 13. Viscosity fields (left column) and temperature isosurfaces (right column) for selected composite yield stress cases. The color bar shows log10(viscosity), which varies between 0.1 and 10,000. The horizontal viscosity slice is at $z = 0.97$. Isosurfaces show where the temperature is 0.1 lower than the geotherm. Yield stress values are (Figures 13a and 13b) 2.8×10^3, (Figures 13c and 13d) 5.7×10^3, (Figures 13e and 13f) 7.1×10^3, (Figures 13g and 13h) 9.9×10^3, (Figures 13i and 13j) 1.4×10^4, (Figures 13k and 13l) 1.7×10^4, and (Figures 13m and 13n) 2.8×10^4.

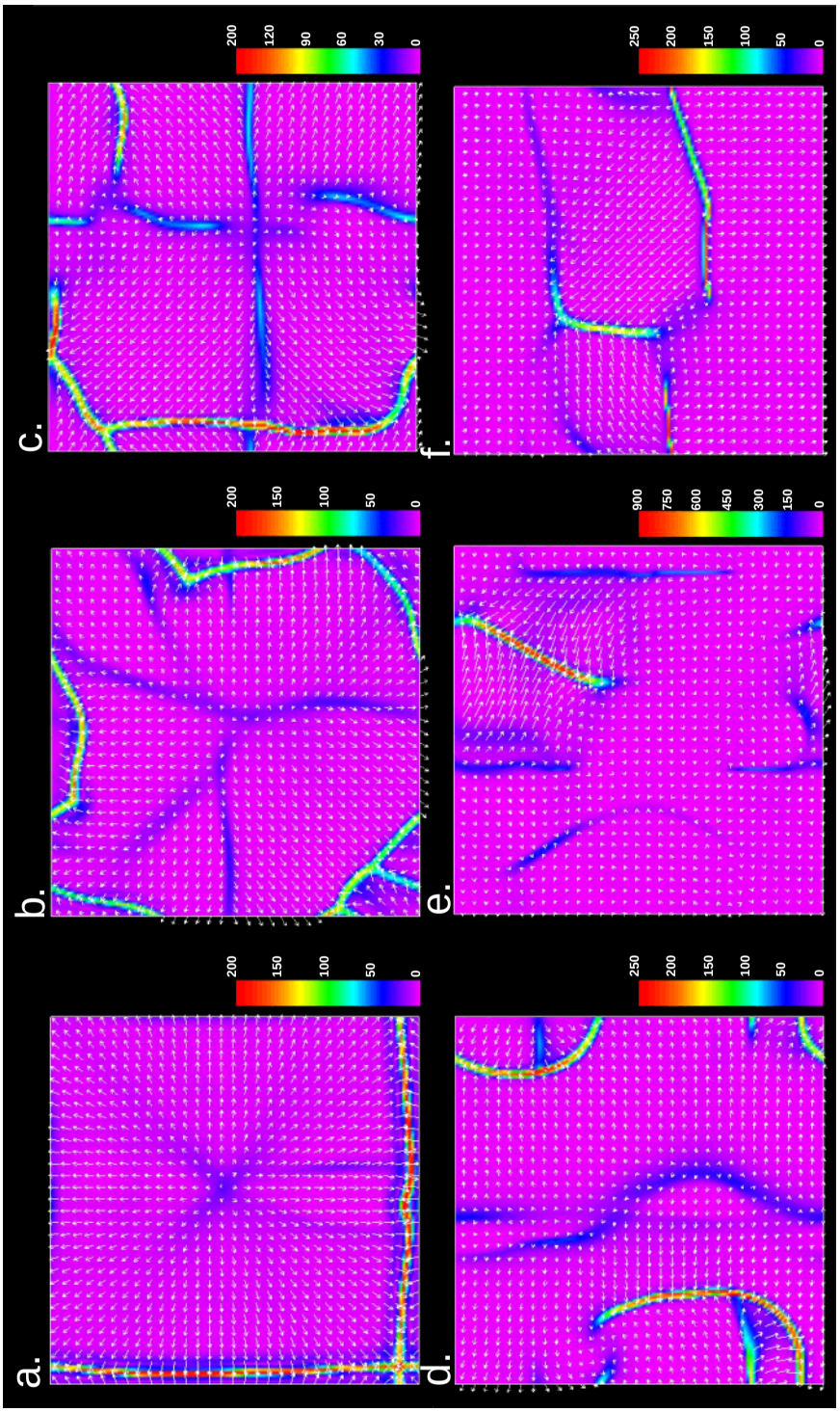
a.
200
150
100
50
0
b.
200
150
100
50
0
c.
200
120
90
60
30
0
d.
250
200
150
100
50
0
e.
900
750
600
450
300
150
0
f.
250
200
150
100
50
0

of Figure 9) are generally higher than those for the constant yield stress cases, even at the lower σ_y' values, and can peak at very high values (for example, 0.86 in Figure 9e). However, since there are no pure transform boundaries, it is not clear how this toroidal motion arises. In this section, toroidal and poloidal surface motions are explicitly presented in order to clarify this issue.

[51] Figure 10 shows a decomposition of the surface velocity field for two cases into poloidal and toroidal components, plotted over horizontal divergence and vertical vorticity, respectively. The first case (left column) has a σ_y' value at the upper end of those which lead to continuous platelike behavior, and an instantaneous toroidal:poloidal ratio of 0.43. Most plate boundaries have a lot of divergence (Figure 10c), whereas vorticity (Figure 10e) is focused along two short "ridge offsets" on the right-hand side and in patches at the complex plate boundary in the lower center, somewhat redolent of calculations with only moderately temperature-dependent viscosity but including viscous dissipation [*Balachandar et al.*, 1995]. The second case (right column) is in a highly episodic regime, and the large ratio of toroidal motion (0.86) is generated by patches of vorticity at each side of a short localized spreading center, caused by horizontal shearing between the small, mobile patch and the surrounding, almost immobile lithosphere.

[52] Plateness P is reasonable in the smoothly evolving regime (0.61–0.74) but rather low in the sluggish-spreading and episodic regimes (0.3–0.4).

3.4.2. Time dependence

[53] The time dependence of cases representing the platelike, sluggish-spreading, convulsive, and immobile-lid regimes is apparent by looking at time series of various quantities. Figure 11 shows indicators of plate behavior, while Figure 12 shows volume-averaged temperature, surface heat flux, and rms velocity. Fairly steady diagnostics at low σ_y' (1.4×10^5, 2.9 MPa/km, Figures 11a and 12a) become more time dependent as σ_y' is increased. In Figures 11b and 12b ($\sigma_y' = 5.7 \times 10^5$, 11.8 MPa/km) the system has settled into the sluggish-spreading mode discussed in the previous paragraph, which is here characterized by intermediate values of mobility and plateness (≈ 0.5) and a low R_{TP}. In the erratic, convulsive case (Figures 11c and 12c) an initial almost immobile lid phase makes a transition to a highly episodic mobile phase, followed by sluggish spreading. For the highest σ_y' (Figures 11d and 12d), some time dependence in the lid deformation is apparent despite very low mobility.

[54] Depth profiles largely show similarities with the constant yield stress cases, except for the new sluggish-spreading mode, an example of which is included in Figure 7. The stress profile indicates that yielding now occurs only in the top part of the domain. In the velocity profiles the subdued surface velocities are clear. Internal temperatures are slightly higher than those for platelike mobility.

3.5. Composite Yield Stress

[55] The cases with combined depth-proportional brittle and constant ductile yield stresses display some markedly different behavior from

Figure 14. Surface strain rate fields for selected cases with composite yield stress values (a) 2.8×10^3, (b) 5.7×10^3, (c) 9.9×10^3, (d) 1.4×10^4, and (e and f) 2.0×10^4 at two different times. Color bars show relative units. Instantaneous diagnostics are (a) $R_{TP} = 0.05$, $P = 0.49$; (b) $R_{TP} = 0.20$, $P = 0.55$; (c) $R_{TP} = 0.24$, $P = 0.60$; (d) $R_{TP} = 0.50$, $P = 0.65$; (e) $R_{TP} = 0.67$, $P = 0.60$; and (f) $R_{TP} = 0.43$, $P = 0.58$.

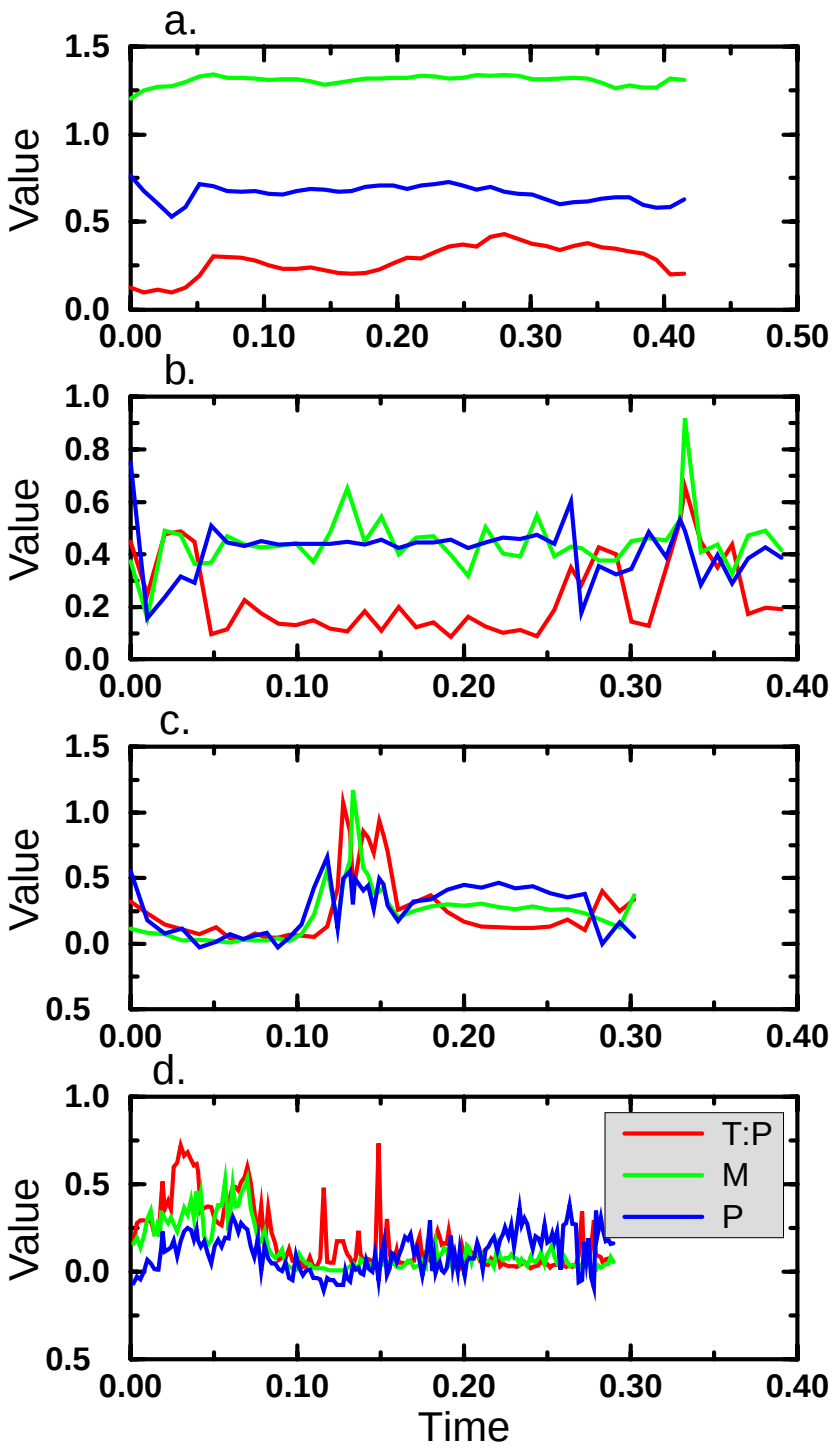

Figure 15. Time series of plate diagnostics: (red) surface toroidal:poloidal ratio, (green) surface mobility, and (blue) plateness for selected cases with composite yield stress values (a) 7.1×10^3, (b) 1.4×10^4, (c) 2.0×10^5, and (d) 2.8×10^5.

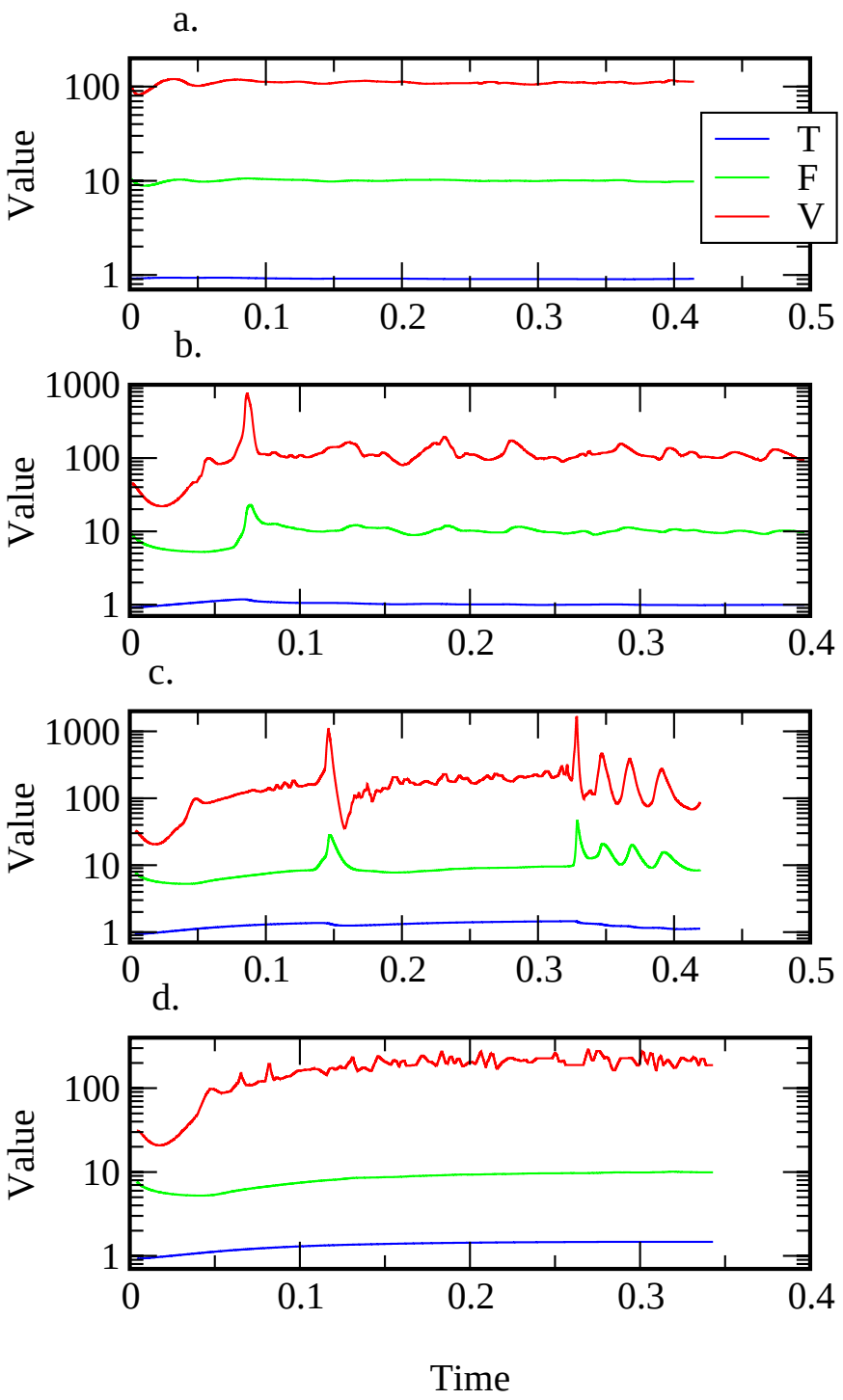

Figure 16. Time series of surface heat flux, volume-averaged rms velocity, and volume-averaged temperature for selected cases with composite yield stress with gradients (a) 7.1×10^3, (b) 1.4×10^4, (c) 2.0×10^5, and (d) 2.8×10^5.

(as well as similarities to) cases with just one or the other, as shown in Figures 13 and 14. They appear most similar to the cases with constant yield stress.

[56] The system evolves smoothly for σ_y values up to $\sim 10^4$ (120 MPa) (top four rows in Figure 13, top row in Figure 14), with well-localized convergent boundaries and passive spreading centers which are diffuse at low σ_y and become sharper as σ_y is increased. Compared to the constant-σ_y cases, the spreading centers seem weaker and more localized, which is due to the effect of the depth-proportional yield stress in shallow regions. At higher σ_y of 1.4×10^4 (168 MPa) the system starts becoming quite time dependent, and by $\sigma_y = 2 \times 10^4$ (240 MPa), plate behavior has become erratic and patchy, with the system being strongly time dependent. This is particularly evident in the two frames illustrated in Figures 13e and 13f, which indicate localized patches of high mobility. Curiously, the highest σ_y value displays a "better" rigid lid than the equivalent constant-σ_y case. Toroidal:poloidal ratios and plateness values display similar trends to the constant-σ_y cases, with R_{TP} perhaps slightly higher.

[57] Time dependence of plate diagnostics (Figure 15) and convective quantities (Figure 16) again bring out these trends. By $\sigma_y = 1.4 \times 10^4$ (168 MPa) (Figures 15b and 16b) the system is quite time dependent, but plate diagnostics have reasonable values. With $\sigma_y = 2 \times 10^4$ (240 MPa) a type of episodic plate tectonics is obtained. Plate diagnostics (Figure 15c) show clearly an early rigid lid, followed by a transition to a mobile lid, followed by a later transition back to a rigid lid, and then back to a mobile lid. Such episodic plate tectonics has been suggested for Venus [*Turcotte*, 1993]. During the mobile lid period, Earth-like plates are not obtained, but rather the erratic, convulsive mode, frames from which are illustrated in Figures 13k–13l and Figures 14e–14f. From this it may be suspected that if a planet such as Venus does undergo episodic plate tectonics, it will not be plate tectonics "as we know it" but something much more episodic and regional.

3.6. Quantitative Scaling of Diagnostics

[58] Previous sections discussed the scaling of behavior with yield stress either qualitatively, for instantaneous frames, or using time series. Here this scaling is better quantified using diagnostics that have been averaged over the second half of each simulation (after the case has overcome any transient behavior associated with initial conditions). Considered are the scaling of time-averaged plate diagnostics and the scaling of time dependence, quantified as the standard deviation of rms velocity and surface heat flow.

3.6.1. Plateness

[59] The dependence of plateness P and other diagnostics on σ_y can be seen in Figure 17 for the three series (constant, depth-proportional, or composite yield stress). For the constant-σ_y cases (Figure 17a), surface mobility M is almost constant with σ_y until the erratic plates regime is reached. However, P and toroidal:poloidal ratio R_{TP} have maxima indicating that the most platelike behavior is obtained with σ_y in the range $\sim 7-9 \times 10^3$ (84–108 MPa). R_{TP} reaches a maximum of ~ 0.45, while plateness reaches ~ 0.7 (indicating that 80% of the deformation occurs in 18% of the surface area).

[60] These trends are more gradual with the depth-proportional yield stress (Figure 17b). Optimum plate character is obtained for σ_y' of $\sim 2 \times 10^5$ (4.1 MPa/km), above which the sluggish-spreading regime exists up to $\sigma_y' \sim 10^6$ (20.7 MPa/km), beyond which the lithosphere finally succumbs. Toroidal:poloidal ratios are Earth-like over a wide range of σ_y'.

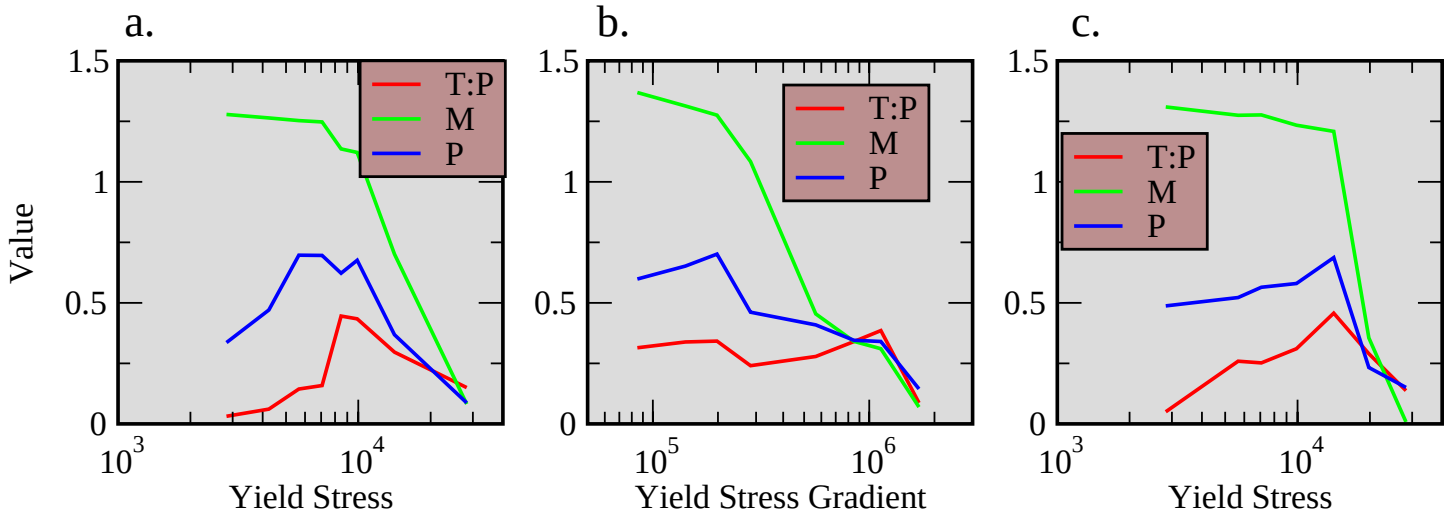

Figure 17. Time-averaged plate diagnostics versus yield stress or yield stress gradient for the three main series of cases: (a) constant yield stress, (b) depth-proportional yield stress, and (c) composite yield stress. Diagnostics are (red) surface toroidal:poloidal ratio, (green) surface mobility, and (blue) plateness.

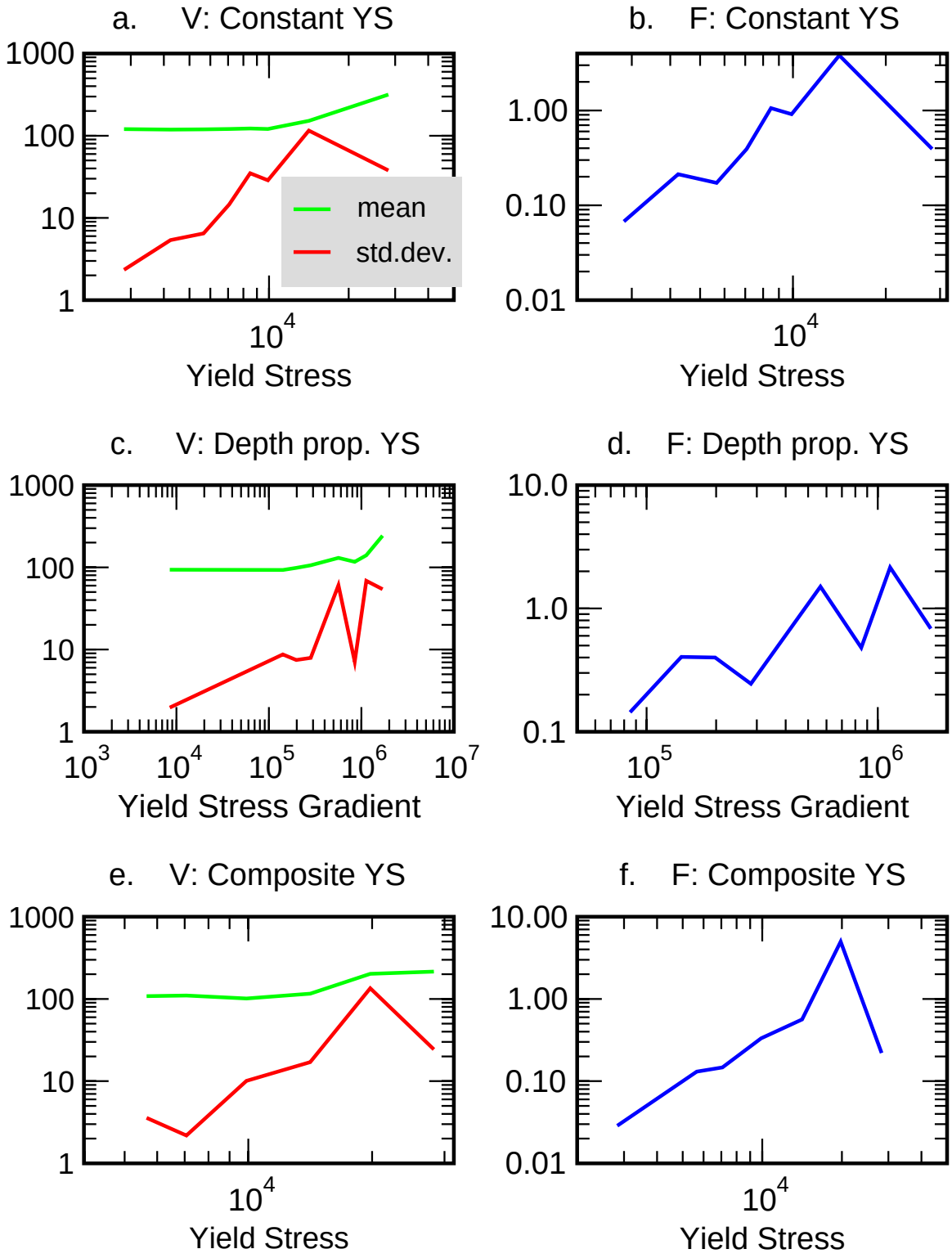
a. V: Constant YS
1000
100
10
1
mean
std.dev.
10^4
Yield Stress
b. F: Constant YS
1.00
0.10
0.01
10^4
Yield Stress
c. V: Depth prop. YS
1000
100
10
1
10^3
10^4
10^5
10^6
10^7
Yield Stress Gradient
d. F: Depth prop. YS
10.0
1.0
0.1
10^5
10^6
Yield Stress Gradient
e. V: Composite YS
1000
100
10
1
10^4
Yield Stress
f. F: Composite YS
10.00
1.00
0.10
0.01
10^4
Yield Stress

[61] In contrast, the arguably most realistic composite yield stress seems to affect a sharper transition between mobility and rigidity than either of the more idealized profiles. Optimum plate diagnostics are obtained for $\sigma_y \sim 1.4 \times 10^4$ (168 MPa), below which reasonable R_{TP} and P are obtained for a wider range of σ_y than with a purely constant yield stress.

3.6.2. Time dependence

[62] The standard deviations of rms (volume-averaged) velocity and surface heat flux plotted in Figure 18 show very well the trends discussed earlier: increasing time dependence for increasing σ_y followed by a decrease in time dependence when the system enters lid immobility. Maximum time dependence is obtained at yield stress values somewhat (e.g., 40%) higher than those which lead to optimum plateness. The peak time dependence is quite dramatic: velocity standard deviations of $\sim$100% and heat flux standard deviations of $\sim$50%. There is some complexity to the depth-proportional yield stress curves (Figures 18c–18d): a minimum in the time-dependence observed at $\sigma_y' = 8.4 \times 10^5$ (17 MPa/km) is due to the system settling into a steady, two-dimensional sluggish-spreading behavior.

[63] The mean (time- and volume-averaged) velocity is also plotted in Figures 18a, 18c, and 18e. The main trend is that velocity increases as the lid becomes less mobile, from $\sim$100 to $\sim$200 or more. Convection beneath an immobile lithosphere needs to be more vigorous to transport the same amount of heat, owing to the lower temperature variations participating in convection. The mean heat flux is not plotted because this is specified by the internal heating rate (10).

3.7. Horizontal Heterogeneity Spectra

[64] The cases with mobile lids generally display the largest horizontal lengthscale flow and thermal structure that is possible in the domain, a displays that does not seem particularly dependent on yield strength. In contrast, constant-viscosity internally heated convection or rigid-lid convection displays very short-wavelength structures. Here this observation is quantified, focusing on the depth-distribution of heterogeneity plotted in the form of spectral heterogeneity maps [*Schubert and Tackley*, 1995; *Tackley et al.*, 1994].

[65] Spectral heterogeneity maps for the constant-viscosity case, for the composite yield-stress case with best plate behavior ($\sigma_y = 10^4$, 120 MPa), and for the rigid lid case (composite $\sigma_y = 2.8 \times 10^4$, 336 MPa) are plotted in Figure 19. With constant viscosity (Figure 19a), high-amplitude heterogeneity is observed in the upper boundary layer (as expected [*Jarvis and Peltier*, 1986]) and with a horizontal spatial frequency of $\sim$1, i.e., the depth of the box. The horizontal frequency depends strongly on Rayleigh number, as shown in the study of *Tackley* [1996b]. A minor peak is observed at the base of the mantle caused by the lateral ponding of downwellings. In the rigid-lid case (Figure 19c) the spectrum is shifted to even shorter wavelengths and is more focused in the region around the base of the lithosphere, rather than being spread through the mantle.

Figure 18. Scaling of velocity rms and standard deviation (left column) and surface heat flux standard deviation (right column) for the three different series, averaged over the second half of each run: (Figures 18a and 18b) constant yield stress, (Figures 18c and 18d) depth-proportional yield stress, and (Figures 18e and 18f) composite yield stress.

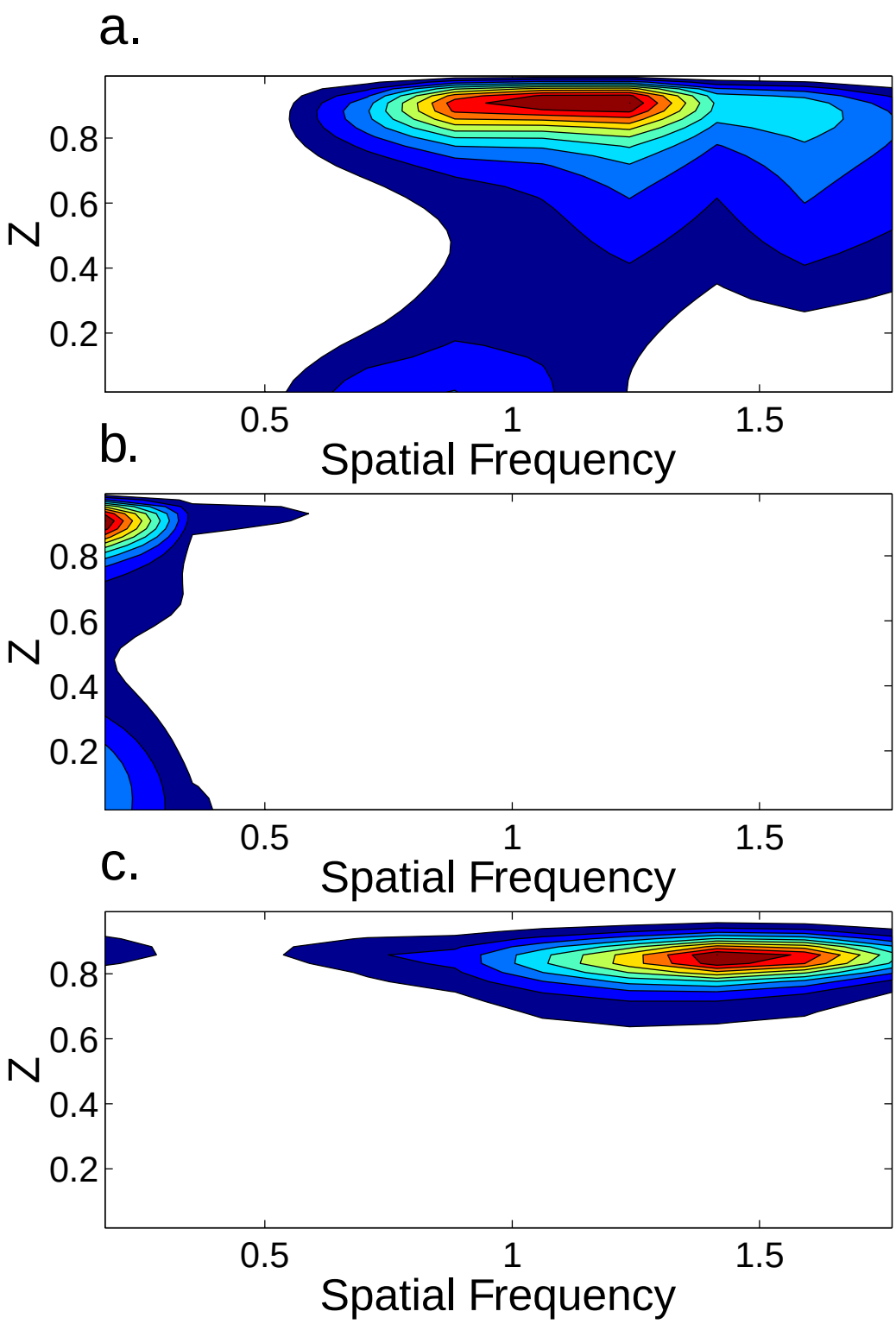
a.
Z
0.8
0.6
0.4
0.2
0.5
1
1.5
Spatial Frequency
b.
Z
0.8
0.6
0.4
0.2
0.5
1
1.5
Spatial Frequency
c.
Z
0.8
0.6
0.4
0.2
0.5
1
1.5
Spatial Frequency

[66] With platelike behavior (Figure 19b) the spectrum is dramatically shifted to lower spatial frequencies (longer wavelength), peaking at the longest wavelength possible. How does this compare to Earth-like values in spherical geometry? The domain width of 8 corresponds to ~24,000 km, whereas the distance around the Earth is 30,600 km at midmantle depth, or 40,000 km at the surface. Thus the wavelength of the box maps to between spherical harmonic degree 2 and degree 1. The wavelength of heterogeneity obtained in the platelike cases is consistent with the dominant wavelength observed in Earth's mantle, which is at degree 2. Of course, caution must be exercised when making such a comparison since the difference in geometry may cause differences in the convection, although previous temperature-dependent viscosity results suggest that these differences may be small [*Ratcliff et al.*, 1997; *Reese et al.*, 1999a].

3.8. Geometry: 2-D Versus 3-D

[67] Since much previous work on plate generation has been performed in 2-D geometry (notably *Moresi and Solomatov* [1998] and *Weinstein and Olson* [1992]), it is useful to consider how the current results would be different in 2-D geometry. For this purpose, two of the cases were also run in two dimensions, using identical parameters and numerical code as in three dimensions. The case illustrated here has a composite yield stress of value 1.4×10^4 (168 MPa) previously illustrated in Figures 13i, 13j, 14d, 15b, and 16b. This case has quite time-dependent behavior but good time-averaged plate diagnostics.

[68] A comparison of the time dependence of velocity and surface heat flux for 2-D and 3-D cases is shown in Figure 20. The 2-D case has markedly larger variations in these quantities than the 3-D cases, by a factor of ~2 or more. Examining a sequence of viscosity snapshots (Figure 21) gives some insight as to the cause of this time dependence. The sequence starts with an immobile-lid frame and shows a downwelling forming from an area of thick lithosphere. Although the downwelling persists for a while, a robust spreading center is not formed, with the location of spreading jumping around. Eventually, the downwelling shuts off (not shown). This cycle repeats itself several times over the simulated time.

4. Discussion and Conclusions

[69] The presented cases show that various types of plate-tectonic-like behavior arise from a relatively simple rheological description. As well as (somewhat) Earth-like plates, some new types of behavior are identified (e.g., incomplete erratic/convulsive, sluggish spreading). These are interesting because, while there may be a tendency to regard models with Earth-like plates as "correct" and other types of mobile lid behavior as "incorrect," it must be recognized that if plate tectonics has occurred on other planets such as Mars and Venus, or the possible billions of extrasolar terrestrial planets, it may well have taken a different form, about which the present results may give some theoretical guidance, insofar as the simple rheological description is reasonable for real planets.

Figure 19. Spectral heterogeneity maps (i.e., the amplitude spectra as a function of vertical coordinate) for (a) constant-viscosity convection, (b) platelike convection with composite yield stress 1.0×10^4, and (c) rigid-lid convection with composite yield stress 2.8×10^4. Contours are equally spaced and normalized to the maximum value.

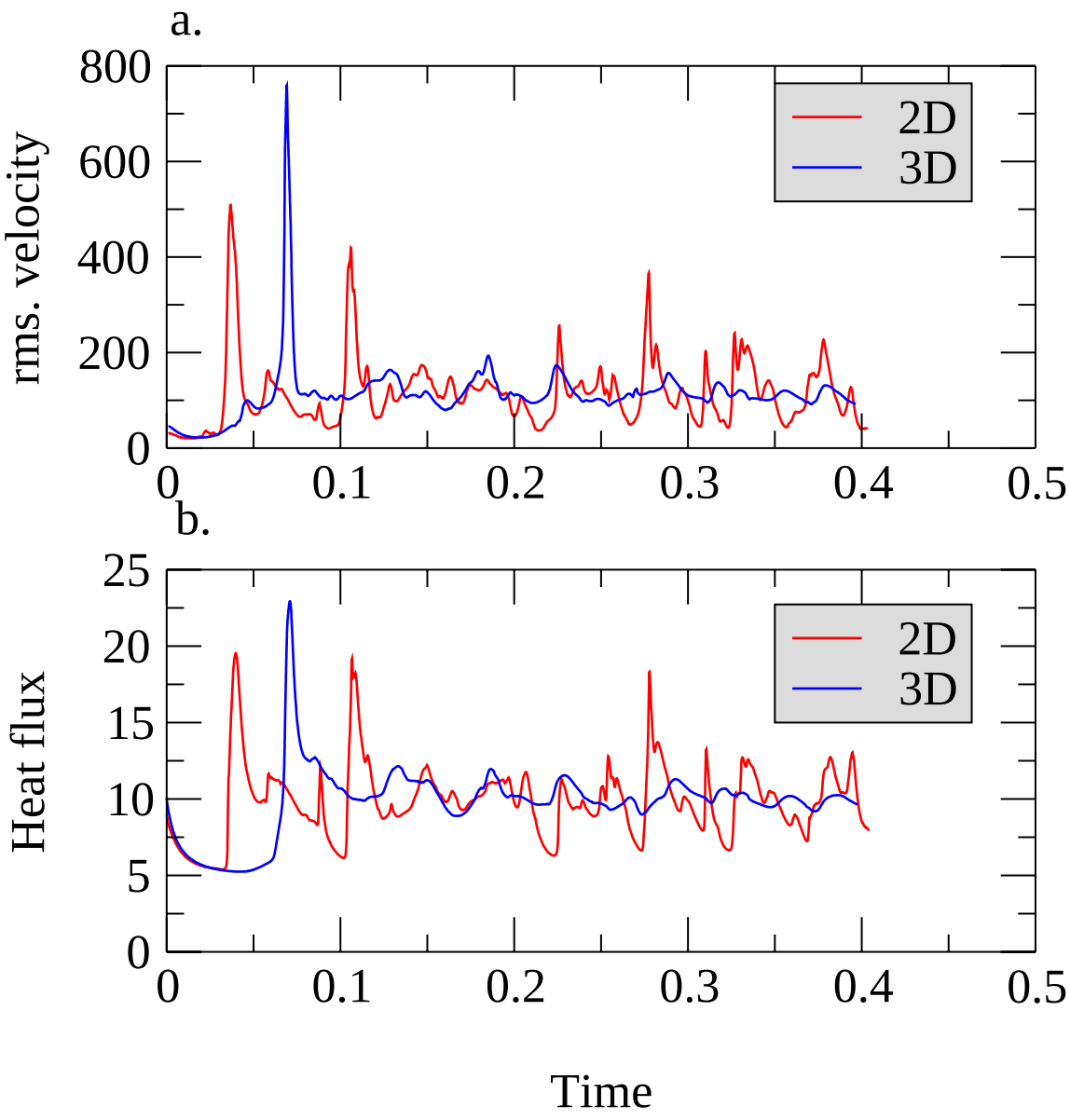

Figure 20. Comparison of time dependence for a 2-D calculation versus a 3-D calculation for a case with composite yield stress value of 1.4×10^4. Identical parameters and code were used for both calculations.

[70] In this section the findings are summarized and successes and shortcomings of the results in producing "Earth-like" plates and the possible broader implications of the results are discussed, together with directions for future research.

4.1. General Findings

[71] Three types of yielding behavior were investigated in the context of purely internally heated convection: constant yield stress ("duc-

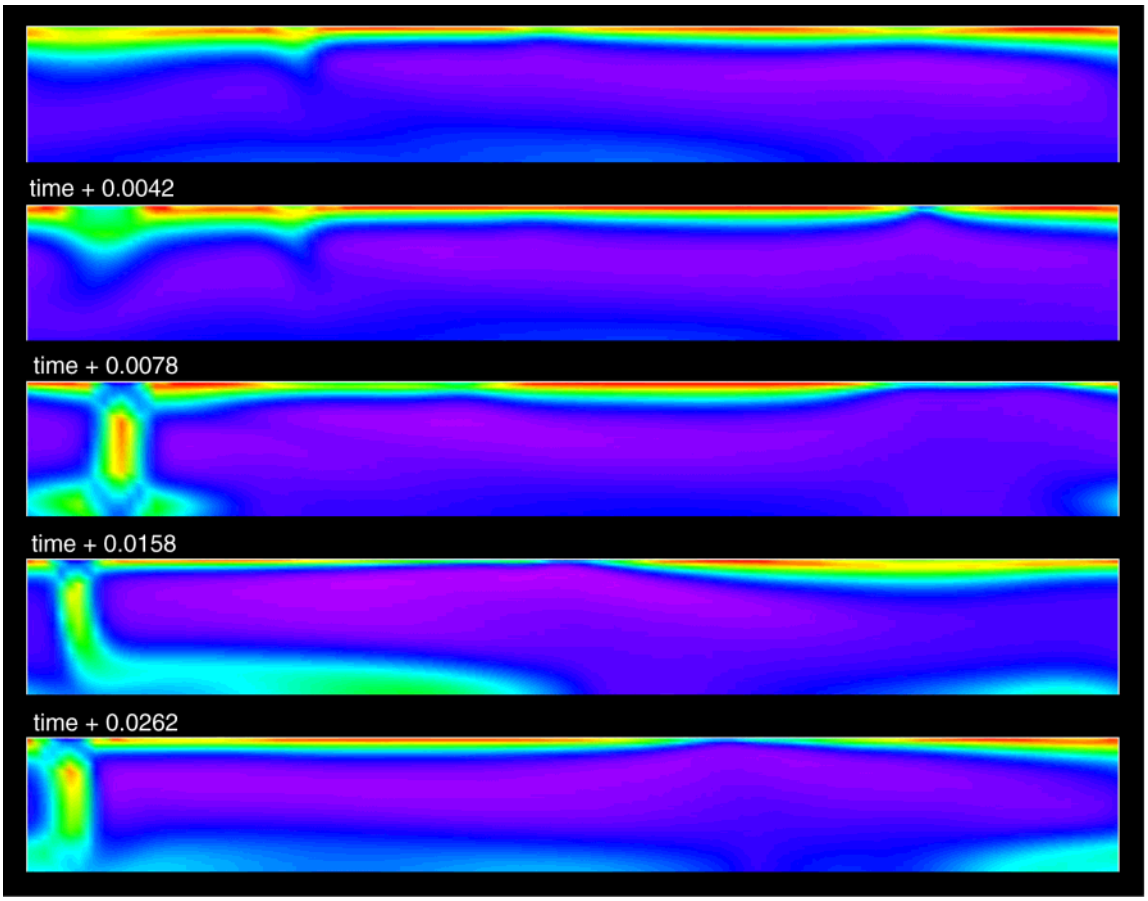

Figure 21. A sequence of frames from a 2-D calculation with composite yield stress value 1.4×10^4, showing time-dependent behavior. The top frame is at a time of 0.3207 into the calculation, and subsequent frames are later, as indicated.

tile" yielding), depth-proportional yield stress ("brittle" deformation), and a combination of the two. The major trends in the results are robust regardless of the behavior used, but the details of the planform, time dependence, etc., are different for each behavior.

[72] Lid mobility occurs over a wide range of yield stress values, but the form of mobility is quite dependent on yield stress value and profile. At low σ_y the tendency is for downwelling weak zones to be localized, divergent centers to be somewhat distributed, plates to be fairly weak, and time dependence to be weak. As σ_y is increased, spreading centers become sharper and plates become stronger, with accompanying increases in the diagnostics plateness P and toroidal:poloidal ratio R_{TP}, which reach a maximum at some optimum σ_y value. As σ_y is increased beyond this optimum value, plate boundaries become incomplete (regionalized) and the system becomes increasingly time dependent ("erratic," "convulsive"). At even higher σ_y the system may switch globally between periods of rigid-lid and regionalized plate behavior, until at high enough σ_y the system is always rigid lid. The basic trend of mobile lid to episodic to rigid lid was first delineated by *Moresi and Solomatov* [1998] in a 2-D aspect-ratio 1 box. Here the same trend is

observed, but a richer range of behaviors is identified both in the continuous plates regime and in the transitional, erratic regime.

[73] Constant-σ_y results are characterized by square or roll-like planforms (at least in a square domain). With depth-proportional σ_y the planform is generally more irregular and the system is more time dependent. A new form of mobile lid behavior, in which spreading centers are localized but downwellings are distributed, exists over a range of high σ_y' values. Combining the two behaviors (depth-proportional at shallow depths but constant at deeper depths) gives arguably the "best" results, with more realistic spreading centers, platelike behavior existing over a wider range of yield stress, and a more abrupt transition to rigid-lid behavior as σ_y is increased.

[74] What are the dimensional values of yield stress needed for platelike behavior? The "best" constant-σ_y case has $\sigma_y = 8.5 \times 10^3$, corresponding to a dimensional stress (see Table 1) of 102 MPa, while the "best" composite-σ_y case has $\sigma_y = 1.0 \times 10^5$, corresponding to 120 MPa. With a pure "brittle" yield stress gradient, the "best" plateness is obtained for nondimensional $\sigma_y' \approx 2 \times 10^5$, corresponding to a rather low 0.83 MPa/km, or 4 MPa/km if further scaled by lithospheric thickness. Such a low value would require exceptionally weak faults, with a friction coefficient of around 0.06, consistent with the findings of *Moresi and Solomatov* [1998]. Pore pressure acts to reduce fault strength, so one possible explanation for the existence of plate tectonics on Earth but not on Venus is the presence of liquid water on Earth [*Moresi and Solomatov*, 1998]. In the absence of substantial fault weakening, semi-brittle, semiductile yielding would be most important for producing plate boundaries. However, the required yield strength is much lower than the "laboratory" value of $\sim$700 MPa (Figure 1). Thus, whether the dominant process is slip on faults or pseudoplastic yielding, the strength required to produce platelike behavior is much lower than laboratory values.

[75] Two-dimensional results are intrinsically more time dependent than three-dimensional results. This is not surprising and seems to be generally true for mantle convection; for example, it was shown for phase-change-modulated "avalanche" convection that 3-D cases display substantially less time dependence in their average diagnostics than 2-D cases [*Tackley et al.*, 1993, 1994], although time-averaged quantities are similar [*Tackley*, 1997].

[76] Where smooth lid mobility occurs, thermal and flow structure adopts a very long wavelength, comparable to the size of the box. What implications does this have for Earth's mantle? The origin of long-wavelength heterogeneity in the mantle has long been debated, since simple thermal convection, particularly with internal heating, has lateral heterogeneity which is too short-wavelength. Various studies have shown the "red-shifting" effect of continents [*Gurnis and Zhong*, 1991; *Tackley*, 2000; *Zhong and Gurnis*, 1993], phase changes [*Tackley*, 1996b], increases in viscosity or thermal expansivity with depth [*Bunge et al.*, 1996; *Hansen et al.*, 1993; *Tackley*, 1996b; *Yuen et al.*, 1991], or the effect of imposed plate motions [*Bunge and Richards*, 1996; *Ratcliff et al.*, 1997]. In the cases presented in this paper, realistic heterogeneity is obtained by a combination of temperature-dependent viscosity and plastic yielding, with no additional physical complexity being necessary.

4.2. Earth-like Plates: Successes and Failures

[77] Many of the presented cases display smoothly evolving platelike behavior which is continuous in space and time and bears

some resemblance to Earth's plate tectonics. Some major successes of these models are the presence of very long-wavelength flow with linear downwellings, the robust presence of passive spreading centers, and toroidal:poloidal ratios which are in the range observed for Earth (despite a lack of pure transform boundaries). Indeed, toroidal:poloidal ratios of order tens of percent seem to be a natural outcome of platelike surface behavior.

[78] The most notable shortcomings of these models with respect to obtaining Earth-like dynamics (other than the obvious lack of continents) are the pervasiveness of double-sided (symmetric) subduction and the lack of pure transform boundaries. Regarding subduction, it is notable that most of Earth's subduction zones occur next to continents, where there is an inherent asymmetry. Preliminary modeling results with buoyant continents included [*Tackley et al.*, 1999] indicate that single-sided subduction at the edge of the continent is a robust outcome, as it is even in simple 2-D isoviscous models with continental rafts [*Zhong and Gurnis*, 1993]. In addition, there has been some argument that Earth's subduction zones have some double-sided or "ablative" component [*Tao and O'Connell*, 1992]. However, there exist some ocean-ocean subduction zones that appear to be single-sided, and it is probable that the present rheological description is missing something. In the present models, subduction zones generally display pairs of weak zones inclined at about 45°. What is "needed" is some mechanism to select just one of these. The present description (Newtonian creep suddenly making a transition to plastic yielding) lacks the progressive softening that is obtained in real silicates through dislocation creep and, in particular, the Peierls mechanism [*Kameyama et al.*, 1999] at higher stresses. Such progressive softening may make it more stressful for plates to bend abruptly through 90° at subduction zones (whereas with pure plastic yielding the stress is the same for all strain rates) and thus favor one inclined subducting plate and one nonsubducting overriding plate.

[79] Regarding pure transform boundaries, it is not clear whether, at a large scale, these are really an essential feature of Earth's plate tectonics. Examining the large-scale pattern of divergence and vorticity of Earth's surface motion (as plotted by, for example, *Bercovici and Wessel* [1994]), most plate boundaries have a mixture of divergent and strike-slip motion, with the only major pure strike-slip boundary being the Pacific:North American boundary in the vicinity of the San Andreas fault. At a local scale, of course, the motion on these mixed boundaries is often accommodated by alternating segments of "pure" motion, as at mid-ocean spreading centers, with their purely divergent ridge segments and purely strike-slip transform offsets. Such behavior is probably due to faulting in the thin young lithosphere. Pure strike-slip boundaries at the large scale may just be transient (coincidental) features in the continually evolving pattern of plate motions and boundaries.

[80] It is interesting that if the yield strength is low enough for platelike behavior to be obtained, then lithospheric effective viscosity tends to be limited by yielding, rather than the intrinsic temperature dependence. For the model this perhaps means that the less-than-realistic viscosity contrast used is not tremendously important, although this requires investigation since some dependence on viscosity contrast was observed in the 2-D study of *Moresi and Solomatov* [1998]. For Earth this implies that if no additional weakening mechanisms were present to further localize deformation to plate boundaries, there could potentially be significant deformation in ocea-

nic plates, as is sometimes observed [*Gordon and Stein*, 1992].

4.3. Future Directions

[81] It is possible to make a long "shopping list" of improvements that could be made to the present model. Two of these, depth-dependent rheology and strain weakening, are investigated in a companion paper to this one (part 2). Of the remaining improvements, the most important may be the inclusion of continents (both crust and cratonic lithosphere) and the inclusion of elasticity and actual brittle failure (not a parameterization using depth-dependent viscoplastic yielding) in the shallow region, which may be the behavior needed to obtain transform segments and possibly single-sided subduction.

[82] Various desired improvements to the rheological model include adding other deformation mechanisms that are known about (power-law dislocation creep, the Peierls mechanism), bringing rheological parameters such as activation energies closer to Earth-like (although this requires a more robust numerical solution scheme), and various complexities such as a viscosity increase after oceanic lithosphere loses its melt, which may help to make oceanic plates more rigid. Furthermore, it will be necessary to include actual weakening mechanisms observed in nature, such as grain-size reduction. The use of a compressible rather than Boussinesq formulation would open up the possibility of shear zone formation through viscous heating. A general problem with including mechanisms that lead to strong localization is that of resolving the resulting small-scale features, perhaps requiring techniques such as adaptive grid refinement.

[83] History dependence will likely be important in obtaining Earth-like plate dynamics. Indeed, a commonly held view is that plate evolution is dominated by long-lived structures, with "new" plate boundaries forming along "preexisting" zones of weakness [*Gurnis et al.*, 2000]. A preliminary exploration of history-dependent weakening is presented in paper 2.

[84] It is important to establish how the present findings scale to more vigorous, Earth-like convective regimes. This was addressed in two dimensions by *Moresi and Solomatov* [1998] and will form the basis of a future paper. Spherical geometry will ultimately be necessary, although preliminary results in spherical geometry (J. R. Baumgardner, personal communication, 1999) show results that are very similar to some of those reported here. The effects of the believed small fraction of basal heating (10–20%) may be important in some circumstances, such as initiating rifting.

Acknowledgments

[85] This research was supported by the NASA/HPCC program, the David and Lucile Packard Foundation, and NASA grant NAG5-3596. Useful discussions were had with Shun Karato, Greg Hirth, David Bercovici, and John Baumgardner, and constructive reviews by Shun Karato, Mike Gurnis, and an anonymous reviewer improved the manuscript.

References

Auth, C., and H. Harder, Multigrid solution of convection problems with strongly variable viscosity, *Geophys. J. Int.*, *137*(3), 793–804, 1999.

Balachandar, S., D. A. Yuen, and D. M. Reuteler, Localization of toroidal motion and shear heating in 3-D high Rayleigh number convection with temperature-dependent viscosity, *Geophys. Res. Lett.*, *22*(4), 477–480, 1995.

Bercovici, D., A simple model of plate generation from mantle flow, *Geophys. J. Int.*, *114*(3), 635–650, 1993.

Bercovici, D., A source-sink model of the generation of plate tectonics from non-Newtonian mantle flow, *J. Geophys. Res.*, *100*(B2), 2013–2030, 1995.

Bercovici, D., Plate generation in a simple model of litho-

sphere-mantle flow with dynamic self-lubrication, *Earth Planet. Sci. Lett.*, *144*(1–2), 41–51, 1996.

Bercovici, D., Generation of plate tectonics from lithosphere-mantle flow and void-volatile self-lubrication, *Earth Planet. Sci. Lett.*, *154*, 139–151, 1998.

Bercovici, D., and P. Wessel, A continuous model of plate tectonic motions, *Geophys. J. Int.*, *119*, 595–610, 1994.

Bercovici, D., G. Schubert, and G. A. Glatzmaier, Influence of heating mode on 3-dimensional mantle convection, *Geophys. Res. Lett.*, *16*(7), 617–620, 1989.

Bercovici, D., Y. Ricard, and M. A. Richards, The relation between mantle dynamics and plate tectonics: A primer, in *Geophysical Monograph Series*, edited by M. A. Richards, R. Gordon, and R. van der Hilst, AGU, Washington, D. C., in press, 2000.

Bird, P., and X. H. Kong, Computer simulations of California tectonics confirm very low strength of major faults, *Geol. Soc. Am. Bull.*, *106*(2), 159–174, 1994.

Bonatti, E., M. Ligi, L. Gasperini, A. Peyve, Y. Raznitsin, and Y. J. Chen, Transform migration and vertical tectonics at the Romanche fracture zone, equatorial Atlantic, *J. Geophys. Res.*, *99*(B11), 21,779–21,802, 1994.

Braun, J., J. Chery, A. Poliakov, D. Mainprice, A. Vauchez, A. Tomassi, and M. Daignieres, A simple parameterization of strain localization in the ductile regime due to grain size reduction: A case study for olivine, *J. Geophys. Res.*, *104*(B11), 25,167–25,181, 1999.

Bunge, H. P., and M. A. Richards, The origin of large-scale structure in mantle convection: Effects of plate motions and viscosity stratification, *Geophys. Res. Lett.*, *23*(21), 2987–2990, 1996.

Bunge, H. P., M. A. Richards, and J. R. Baumgardner, Effect of depth-dependent viscosity on the planform of mantle convection, *Nature*, *379*(6564), 436–438, 1996.

Byerlee, J., The brittle-ductile transition in rocks, *J. Geophys. Res.*, *73*, 4741–4750, 1968.

Christensen, U., Convection with pressure-dependent and temperature-dependent non-Newtonian rheology, *Geophys. J. R. Astron. Soc.*, *77*(2), 343–384, 1984a.

Christensen, U. R., Heat transport by variable viscosity convection and implications for the Earth's thermal evolution, *Phys. Earth Planet. Inter.*, *35*(4), 264–282, 1984b.

Christensen, U., and H. Harder, 3-D convection with variable viscosity, *Geophys. J. Int.*, *104*(1), 213–226, 1991.

Cserepes, L., Numerical studies of non-Newtonian mantle convection, *Phys. Earth Planet. Inter.*, *30*(1), 49–61, 1982.

Davies, G. F., Mantle convection model with a dynamic plate—Topography, heat flow and gravity anomalies, *Geophys. J. Int.*, *98*(3), 461–464, 1989.

Davies, G. F., Punctuated tectonic evolution of the Earth, *Earth Planet. Sci. Lett.*, *136*(3–4), 363–379, 1995.

Drury, M. R., R. L. M. Vissers, D. Vanderwal, and E. H. H. Strating, Shear localization in upper mantle peridotites, *Pure Appl. Geophys.*, *137*(4), 439–460, 1991.

Dumoulin, C., D. Bercovici, and P. Wessel, A continuous plate tectonic model using geophysical data to estimate plate margin widths, with a seismicity-based example, *Geophys. J. Int.*, *133*(2), 379–389, 1998.

Fleitout, L., and C. Froidevaux, Thermal and mechanical evolution of shear zones, *J. Struct. Geol.*, *2*, 159–164, 1980.

Gable, C. W., R. J. O'Connell, and B. J. Travis, Convection in three dimensions with surface plates: Generation of toroidal flow, *J. Geophys. Res.*, *96*(B5), 8391–8405, 1991.

Gordon, R. G., and S. Stein, Global tectonics and space geodesy, *Science*, *256*(5055), 333–342, 1992.

Grasset, O., and E. M. Parmentier, Thermal convection in a volumetrically heated, infinite Prandtl number fluid with strongly temperature-dependent viscosity: Implications for planetary evolution., *J. Geophys. Res.*, *103*, 18,171–18,181, 1998.

Gurnis, M., Large-scale mantle convection and the aggregation and dispersal of supercontinents, *Nature*, *332*(6166), 695–699, 1988.

Gurnis, M., and S. Zhong, Generation of long wavelength heterogeneity in the mantle by the dynamic interaction between plates and convection, *Geophys. Res. Lett.*, *18*(4), 581–584, 1991.

Gurnis, M., S. Zhong, and J. Toth, On the competing roles of fault reactivation and brittle failure in generating plate tectonics from mantle convection, in *Geophysical Monograph Series*, edited by M. A. Richards, R. Gordon, and R. van der Hilst, AGU, Washington, D.C., in press, 2000.

Hager, B. H., and R. J. O'Connell, Subduction zone dip angles and flow driven by plate motion, *Tectonophysics*, *50*, 111–133, 1978.

Hager, B. H., and R. J. O'Connell, A simple model of plate dynamics and mantle convection, *J. Geophys. Res.*, *86*(B6), 4843–4867, 1981.

Hager, B. H., and M. A. Richards, Long-wavelength variations in Earth's geoid—Physical models and dynamical implications, *Philos. Trans. R. Soc. London, Ser. A*, *328*(1599), 309–327, 1989.

Hansen, U., D. A. Yuen, S. E. Kroening, and T. B. Larsen, Dynamic consequences of depth-dependent thermal expansivity and viscosity on mantle circulations and thermal structure, *Phys. Earth Planet. Inter.*, *77*(3–4), 205–223, 1993.

Houseman, G., The dependence of convection planform on mode of heating, *Nature*, *332*(6162), 346–349, 1988.

Jarvis, G. T., and W. R. Peltier, Lateral heterogeneity in the convecting mantle, *J. Geophys. Res.*, *91*(B1), 435–451, 1986.

Jin, D. H., S. Karato, and M. Obata, Mechanisms of shear localization in the continental lithosphere—Inference from the deformation microstructures of peridotites from the Ivrea zone, northwestern Italy, *J. Struct. Geol.*, *20*(2–3), 195–209, 1998.

Kameyama, M., D. A. Yuen, and H. Fujimoto, The interaction of viscous heating with grain-size dependent rheology in the formation of localized slip zones, *Geophys. Res. Lett.*, *24*(20), 2523–2526, 1997.

Kameyama, M., D. A. Yuen, and S.-I. Karato, Thermal-mechanical effects of low-temperature plasticity (the Peierls mechanism) on the deformation of a viscoelastic shear zone, *Earth Planet. Sci. Lett.*, *168*(1–2), 159–172, 1999.

King, S. D., and B. H. Hager, Subducted slabs and the geoid, 1, Numerical experiments with temperature-dependent viscosity, *J. Geophys. Res.*, *99*(B10), 19,843–19,852, 1994.

Kirby, S. H., Tectonic stresses in the lithosphere: Constraints provided by the experimental deformation of rocks, *J. Geophys. Res.*, *85*(B11), 6353–6363, 1980.

Kohlstedt, D. L., B. Evans, and S. J. Mackwell, Strength of the lithosphere—Constraints imposed by laboratory experiments, *J. Geophys. Res.*, *100*(B9), 17,587–17,602, 1995.

Kopitzke, U., Finite element convection models: Comparison of shallow and deep mantle convection, and temperatures in the mantle, *J. Geophys.*, *46*, 97–121, 1979.

Lithgow-Bertelloni, C., M. A. Richards, Y. Ricard, R. J. O'Connell, and D. C. Engebretson, Toroidal-poloidal partitioning of plate motions since 120 Ma, *Geophys. Res. Lett.*, *20*(5), 375–378, 1993.

Lowman, J. P., and G. T. Jarvis, Effects of mantle heat source distribution on supercontinent stability, *J. Geophys. Res.*, *104*(B6), 12,746–12,773, 1999.

Moresi, L. N., and V. S. Solomatov, Numerical investigation of 2d convection with extremely large viscosity variations, *Phys. Fluids*, *7*(9), 2154–2162, 1995.

Moresi, L., and V. Solomatov, Mantle convection with a brittle lithosphere—Thoughts on the global tectonic styles of the Earth and Venus, *Geophys. J. Int.*, *133*(3), 669–682, 1998.

Ogawa, M., G. Schubert, and A. Zebib, Numerical simulations of 3-dimensional thermal convection in a fluid with strongly temperature-dependent viscosity, *J. Fluid Mech.*, *233*, 299–328, 1991.

Olson, P., and D. Bercovici, On the equipartition of kinetic energy in plate tectonics, *Geophys. Res. Lett.*, *18*(9), 1751–1754, 1991.

Parmentier, E. M., C. Sotin, and B. J. Travis, Turbulent 3-D thermal convection in an infinite Prandtl number, volumetrically heated fluid—Implications for mantle dynamics, *Geophys. J. Int.*, *116*(2), 241–251, 1994.

Pili, E., Y. Ricard, J. M. Lardeaux, and S. M. F. Sheppard, Lithospheric shear zones and mantle-crust connections, *Tectonophys.*, *280*(1–2), 15–29, 1997.

Ratcliff, J. T., G. Schubert, and A. Zebib, Effects of temperature-dependent viscosity on thermal convection in a spherical shell, *Physica D*, *97*(1–3), 242–252, 1996.

Ratcliff, J. T., P. J. Tackley, G. Schubert, and A. Zebib, Transitions in thermal convection with strongly variable viscosity, *Phys. Earth Planet. Inter.*, *102*, 201–212, 1997.

Reese, C. C., V. S. Solomatov, and L.-N. Moresi, Heat transport efficiency for stagnant lid convection with dislocation viscosity: Application to Mars and Venus, *J. Geophys. Res.*, *103*(E6), 13,643–13,657, 1998.

Reese, C. C., V. S. Solomatov, J. R. Baumgardner, and W.-S. Yang, Stagnant lid convection in a spherical shell, *Phys. Earth Planet. Inter.*, *116*, 1–7, 1999a.

Reese, C. C., V. S. Solomatov, and L.-N. Moresi, Non-Newtonian stagnant lid convection and magmatic resurfacing on Venus, *Icarus*, *139*(1), 67–80, 1999b.

Regenauer-Lieb, K., Dilatant plasticity applied to Alpine collision: Ductile void growth in the intraplate area beneath the Eifel volcanic field, *J. Geodyn.*, *27*(1), 1–21, 1999.

Regenauer-Lieb, K., and D. A. Yuen, Rapid conversion of elastic energy into plastic shear heating during incipient necking of the lithosphere, *Geophys. Res. Lett.*, *25*(14), 2737–2740, 1998.

Ribe, N. M., The dynamics of thin shells with variable viscosity and the origin of toroidal flow in the mantle, *Geophys. J. Int.*, *110*(3), 537–552, 1992.

Ricard, Y., C. Vigny, and C. Froidevaux, Mantle heterogeneities, geoid, and plate motion — A Monte-Carlo inversion, *J. Geophys. Res.*, *94*(B10), 13,739–13,754, 1989.

Schubert, G., and P. J. Tackley, Mantle dynamics: The strong control of the spinel-perovskite transition at a depth of 660 km, *J. Geodyn.*, *20*(4), 417–428, 1995.

Schubert, G., and D. A. Yuen, Shear heating instability in the Earth's upper mantle, *Tectonophysics*, *50*, 197–205, 1988.

Scotese, C. R., Jurassic and Cretaceous plate tectonic reconstructions, *Palaeogeogr. Palaeoclimatol. Palaeoecol.*, *87*(1–4), 493–501, 1991.

Solomatov, V. S., Scaling of temperature-dependent and stress-dependent viscosity convection, *Phys. Fluids*, *7*(2), 266–274, 1995.

Solomatov, V. S., and L. N. Moresi, Stagnant lid convection on Venus, *J. Geophys. Res.*, *101*(E2), 4737–4753, 1996.

Sorensen, K., Growth and dynamics of the Nordre-Stromfjord shear zone, *J. Geophys. Res.*, *88*(B4), 3419–3437, 1983.

Tackley, P. J., Effects of strongly temperature-dependent viscosity on time-dependent, 3-dimensional models of mantle convection, *Geophys. Res. Lett.*, *20*(20), 2187–2190, 1993.

Tackley, P. J., Three-dimensional models of mantle convection: Influence of phase transitions and temperature-dependent viscosity, Ph.D. thesis, Calif. Inst. of Technol., Pasadena, 1994.

Tackley, P. J., Effects of strongly variable viscosity on three-dimensional compressible convection in planetary mantles, *J. Geophys. Res.*, *101*, 3311–3332, 1996a.

Tackley, P. J., On the ability of phase transitions and viscosity layering to induce long-wavelength heterogeneity in the mantle, *Geophys. Res. Lett.*, *23*, 1985–1988, 1996b.

Tackley, P. J., Effects of phase transitions on three-dimensional mantle convection, in *The Fluid Mechanics of Astrophysics and Geophysics,* vol. 5, *The Doornbos Volume*, edited by D. Crossley, pp. 273–336, Gordon and Breach, Newark, N.J., 1997.

Tackley, P. J., Self-consistent generation of tectonic plates in three-dimensional mantle convection, *Earth Planet. Sci. Lett.*, *157*, 9–22, 1998.

Tackley, P. J., The quest for self-consistent incorporation of plate tectonics in mantle convection, in *Geophysical Monograph Series*, edited by M. A. Richards, R. Gordon, and R. van der Hilst, AGU, Washington, D. C., in press, 2000.

Tackley, P. J., D. J. Stevenson, G. A. Glatzmaier, and G. Schubert, Effects of an endothermic phase transition at 670 km depth in a spherical model of convection in the Earth's mantle, *Nature*, *361*(6414), 699–704, 1993.

Tackley, P. J., D. J. Stevenson, G. A. Glatzmaier, and G. Schubert, Effects of multiple phase transitions in a 3-dimensional spherical model of convection in Earth's mantle, *J. Geophys. Res.*, *99*(B8), 15,877–15,901, 1994.

Tackley, P. J., J. R. Baumgardner, G. A. Glatzmaier, P. Olson, and T. Clune, Three-dimensional spherical simulations of convection in Earth's mantle and core using massively-parallel computers, paper presented at 1999 Advanced Simulation Technologies Conference, High Performance Computing Symposium, Soc. for Comput. Simul. Int., San Diego, Calif. 1999.

Tao, W. C., and R. J. O'Connell, Ablative subduction—A 2-sided alternative to the conventional subduction model, *J. Geophys. Res.*, *97*(B6), 8877–8904, 1992.

Travis, B., S. Weinstein, and P. Olson, 3-dimensional convection planforms with internal heat generation, *Geophys. Res. Lett.*, *17*(3), 243–246, 1990.

Trompert, R. A., and U. Hansen, The application of a finite-volume multigrid method to 3-dimensional flow problems in a highly viscous fluid with a variable viscosity, *Geophys. Astrophys. Fluid Dyn.*, *83*(3–4), 261–291, 1996.

Trompert, R., and U. Hansen, Mantle convection simulations with rheologies that generate platelike behavior, *Nature*, *395*(6703), 686–689, 1998a.

Trompert, R. A., and U. Hansen, On the Rayleigh number dependence of convection with a strongly temperature-dependent viscosity, *Phys. Fluids*, *10*(2), 351–360, 1998b.

Turcotte, D. L., An episodic hypothesis for Venusian tectonics, *J. Geophys. Res.*, *98*(E9), 17,061–17,068, 1993.

Turcotte, D. L., and G. Schubert, *Geodynamics: Applications of Continuum Physics to Geological Problems,* John Wiley, New York, 1982.

Vissers, R. L. M., M. R. Drury, E. H. H. Strating, C. J. Spiers, and D. Vanderwal, Mantle shear zones and their effect on lithosphere strength during continental breakup, *Tectonophysics*, *249*(3–4), 155–171, 1995.

Weinstein, S. A., Thermal convection in a cylindrical annulus with a non-Newtonian outer surface, *Pure Appl. Geophys.*, *146*(3–4), 551–572, 1996.

Weinstein, S. A., The effect of convection planform on the toroidal-poloidal energy ratio, *Earth Planet. Sci. Lett.*, *155*(1–2), 87–95, 1998.

Weinstein, S. A., and P. L. Olson, Thermal convection with non-Newtonian plates, *Geophys. J. Int.*, *111*(3), 515–530, 1992.

Yang, W.-S., and J. R. Baumgardner, A matrix-dependent transfer multigrid method for strongly variable viscosity infinite Prandtl number thermal convection, *Geophys. Astrophys. Fluid Dyn.*, in press, 2000.

Yuen, D. A., L. Fleitout, G. Schubert, and C. Froidevaux, Shear deformation zones along major transform faults and subducting slabs, *Geophys. J. R. Astron. Soc.*, *54*, 93–119, 1978.

Yuen, D. A., F. J. Spera, U. Hansen, D. A. Yuen, and S. E. Kroening, Effects of depth-dependent thermal expansivity on mantle circulations and lateral thermal anomalies, *Phys. Rev. B Condens. Matter*, *44*(5), 2108–2121, 1991.

Zhong, S., and M. Gurnis, Dynamic feedback between a continent-like raft and thermal convection, *J. Geophys. Res.*, *98*(B7), 12,219–12,232, 1993.

Zhong, S., and M. Gurnis, Towards a realistic simulation of plate margins in mantle convection, *Geophys. Res. Lett.*, *22*(8), 981–984, 1995.

Zhong, S., M. Gurnis, and L. Moresi, Role of faults, nonlinear rheology, and viscosity structure in generating plates from instantaneous mantle flow models, *J. Geophys. Res.*, *103*(B7), 15,255–15,268, 1998.